

CANCER

MIBI-TOF: A multiplexed imaging platform relates cellular phenotypes and tissue structure

Leeat Keren^{1*}, Marc Bosse^{1*}, Steve Thompson¹, Tyler Risom¹, Kausalia Vijayaragavan¹, Erin McCaffrey^{1,2}, Diana Marquez¹, Roshan Angoshtari¹, Noah F. Greenwald^{1,3}, Harris Fienberg¹, Jennifer Wang¹, Neeraja Kambham¹, David Kirkwood¹, Garry Nolan⁴, Thomas J. Montine¹, Stephen J. Galli¹, Robert West¹, Sean C. Bendall^{1*}, Michael Angelo^{1*†}

Understanding tissue structure and function requires tools that quantify the expression of multiple proteins while preserving spatial information. Here, we describe MIBI-TOF (multiplexed ion beam imaging by time of flight), an instrument that uses bright ion sources and orthogonal time-of-flight mass spectrometry to image metal-tagged antibodies at subcellular resolution in clinical tissue sections. We demonstrate quantitative, full periodic table coverage across a five-log dynamic range, imaging 36 labeled antibodies simultaneously with histochemical stains and endogenous elements. We image fields of view up to 800 $\mu\text{m} \times 800 \mu\text{m}$ at resolutions down to 260 nm with sensitivities approaching single-molecule detection. We leverage these properties to interrogate intrapatient heterogeneity in tumor organization in triple-negative breast cancer, revealing regional variability in tumor cell phenotypes in contrast to a structured immune response. Given its versatility and sample back-compatibility, MIBI-TOF is positioned to leverage existing annotated, archival tissue cohorts to explore emerging questions in cancer, immunology, and neurobiology.

INTRODUCTION

Our understanding of complex cellular systems has evolved in lock-step with the development of increasingly sophisticated analytical approaches to interrogate them. In particular, understanding how the phenotype of individual cells relates to the function of the multicellular structures they comprise requires the ability to quantify the spatial distribution of multiple proteins across large regions of intact tissue at subcellular resolution. Until recently, routine laboratory assays could only satisfy one of these two requirements—either measuring expression of one or two proteins in intact specimens (1) or many genes or gene products in cell suspensions from dissociated tissues (2, 3). This disparity between our conceptual understanding of multicellularity and the experimental tools at our disposal has driven recent developments of multiplexed imaging modalities based on cyclic fluorescent staining, sequencing, or the use of mass reporters (4–19). These innovations have advanced our understanding of how single-cell phenotypes relate to global function in solid tissue. However, these approaches have been limited in sensitivity and throughput and often require specialized sample preparation that limits broader use. Thus, there is an unmet need for a multiplexed imaging modality that is sensitive, robust, high throughput, and back compatible with standard tissue processing techniques.

In previous work, we demonstrated a proof of principle for multiplexed ion beam imaging (MIBI) (4), a method that uses elementally labeled antibodies and secondary ion mass spectrometry (SIMS) to achieve multiplexed imaging with high resolution and sensitivity in archival human tissue biopsies (Fig. 1A). Tissue sections are stained with a mixture of antibodies with cognate elemental reporters. SIMS is then used to interrogate the sample using a primary ion beam com-

posed of atomic ions (i.e., O_2^+) that is focused to a small spot size and rastered across the tissue section. The primary ion beam sputters the elemental reporters and tissue-endogenous elements, releasing secondary ions that are quantified through a mass spectrometer. This ultimately results in a high-dimensional image, depicting the expression of multiple proteins. The imaging resolution and sensitivity of SIMS make it especially suited for tissue imaging. SIMS is among the most sensitive methods known for elemental analysis, where, depending on the element of interest, as few as five atoms can be detected (20, 21). In addition, SIMS can achieve imaging resolutions as low as 10 nm, exceeding the capabilities of not only laser ablation mass spectrometry by >100-fold (22) but also the light diffraction limit, thus permitting super-resolution imaging.

Most of the SIMS instruments can be classified into two general categories: dynamic or static. Dynamic SIMS instruments, like the one we have used previously (4) (NanoSIMS 50 L, Cameca), continuously sputter the sample with a primary beam that, in turn, produces a continuous stream of secondary ions (23). The secondary ions are mass separated by a magnetic sector, where each mass of interest is projected onto a separate ion detector. Continuous sputtering maximizes the rate of sample milling, which, in turn, minimizes acquisition time for a given amount of material. However, the use of a magnetic sector limits the number of masses that can be detected in parallel to the number of ion detectors. Due to cost and complexity, the number of ion detectors does not exceed seven in any commercial instrument. Moreover, mass calibration, primary and secondary ion optics alignment, and sample loading are often complicated and tedious.

In contrast, instead of a magnetic sector, ion detection in static SIMS instruments is achieved with a linear time-of-flight (TOF) mass spectrometer, where mass is calculated by determining the time it takes for each ion to arrive at a single ion detector relative to a common start time. Because discrete detectors for each mass are not required in static SIMS, the entire elemental mass spectrum is thereby acquired for each pixel in the image. However, linear TOF analyzers common to static SIMS require 20 μs or more to acquire a mass spectrum for

Copyright © 2019
The Authors, some
rights reserved;
exclusive licensee
American Association
for the Advancement
of Science. No claim to
original U.S. Government
Works. Distributed
under a Creative
Commons Attribution
NonCommercial
License 4.0 (CC BY-NC).

¹Department of Pathology, Stanford University, Stanford, CA. ²Immunology Program, Stanford University School of Medicine, Stanford, CA. ³Cancer Biology Program, Stanford University School of Medicine, Stanford, CA. ⁴Department of Microbiology and Immunology, Stanford University, Stanford, CA.

*These authors contributed equally to this work.

†Corresponding author. Email: mangelo0@stanford.edu

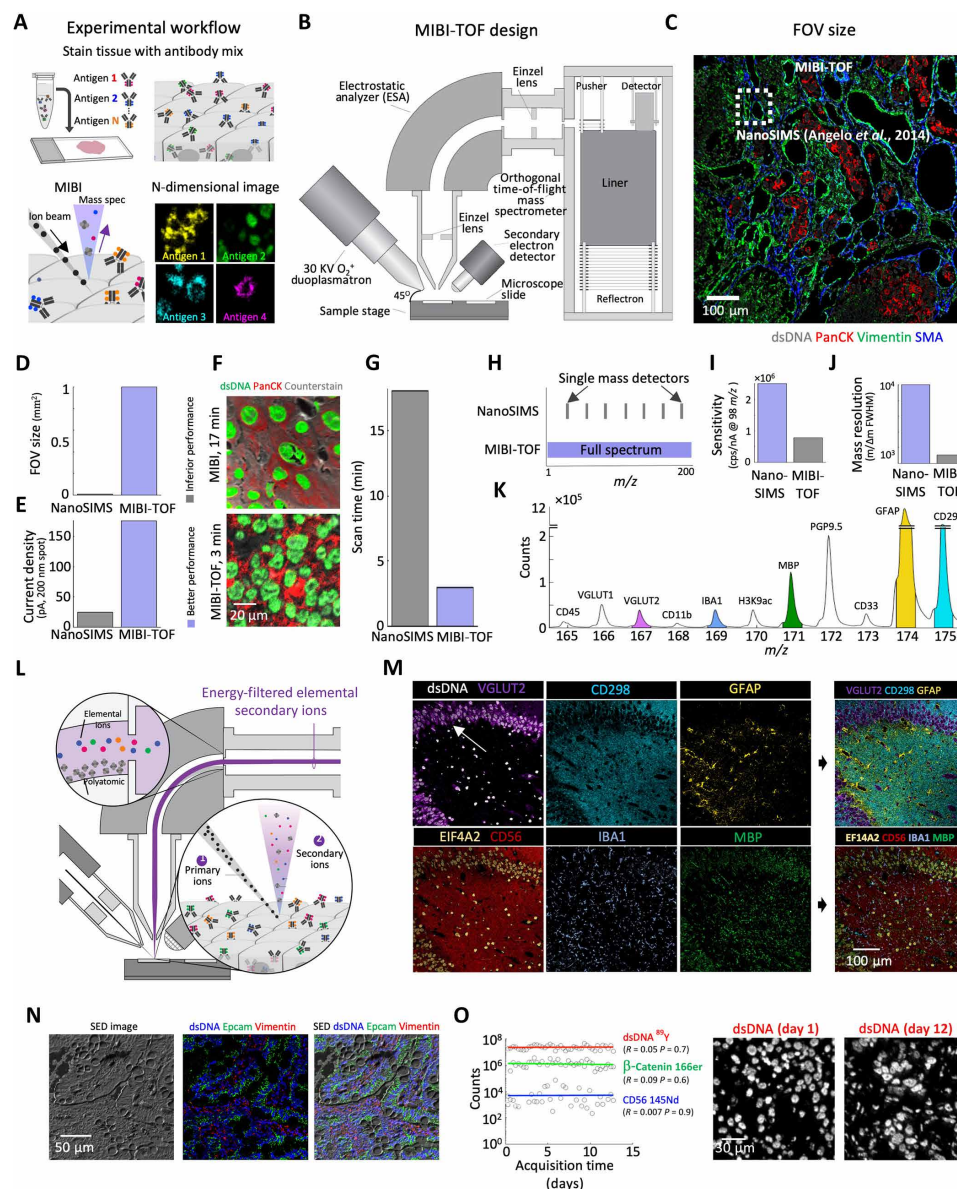


Fig. 1. MIBI-TOF is designed for high-throughput, highly multiplexed tissue imaging. (A) MIBI-TOF experimental procedure. A tissue section is stained with a mix of antibodies, each labeled with a unique metal isotope. To detect the isotopes, the tissue is rastered, pixel by pixel, by primary charged ions. Secondary ions, released from the tissue, are measured by time-of-flight mass spectrometry (TOF-MS) to generate an N-dimensional image. (B) MIBI-TOF instrumentation. MIBI-TOF is composed of several key parts: the sample stage, where slides are loaded into the instrument; a primary ion source, which shoots charged particles at the specimen, releasing secondary ions; an electrostatic analyzer (ESA), which filters secondary ions; a TOF mass spectrometer, which measures element abundance; and a raster scanner, which rasters the primary ion beam across the selected FOV in a stepwise pattern. (C) An 800 μm × 800 μm FOV of breast carcinoma imaged by MIBI-TOF. Inset depicts a 100 μm × 100 μm region, which can be imaged by NanoSIMS 50 L. (D to J) Comparison of various parameters for NanoSIMS 50 L and MIBI-TOF. Purple indicates more favorable values. (D) FOV sizes. (E) Current density (current per spot size). (F) FOVs (100 μm × 100 μm) were stained and visualized by NanoSIMS (top, 17 min) and MIBI-TOF (bottom, 3 min). Counterstain for the top image was hematoxylin and for the bottom image was carbon. (G) Scan times for the FOVs shown in (F). (H) Schematic depicting the mass range (x axis) measured by NanoSIMS and MIBI-TOF. Whereas the NanoSIMS uses a magnetic sector that inherently limits the number of detectable masses to the number of detectors (less than seven), MIBI-TOF acquires the entire spectrum from 1 to 240 m/z. (I) Sensitivity, measured by scanning a molybdenum standard. (J) Mass resolution (mass divided by full width of the peak at half mass). (K) FFPE human hippocampus was stained with a panel of 40 antibodies, and a 500 μm × 500 μm FOV was imaged by MIBI-TOF. The mass spectrum in the range of 165 to 175 m/z, summed over the entire image, is shown. (L) Energy filtering by MIBI-TOF. The primary ion beam hits the sample, releasing both elemental isotopes and polyatomic adducts, which may overlap in mass. Polyatomics are energy-filtered by the ESA, which prevents them from entering the TOF. Einzel lenses in the secondary ion optics are omitted for clarity. (M) Multiplexed staining for dsDNA, VGLUT2, CD298, glial fibrillary acidic protein (GFAP), EIF4A2, IBA1, and myelin basic protein (MBP), corresponding to the spectrum in (K). (N) A 200 μm × 200 μm FOV of human gastrointestinal (GI) tract was stained with a 20-plex panel and scanned with MIBI-TOF. Left: Secondary electron density (SED) image. Middle: Antibody staining for dsDNA (blue), Epcam (green), and vimentin (red). Right: Overlay of antibody stains with SED image. (O) A tissue microarray of biopsies from 41 TNBC patients was stained with a panel of 36 antibodies. FOVs (800 μm × 800 μm) were measured continuously, 24 hours a day for 12 consecutive days, with no tuning of the machine. Left: For each biopsy, the intensities, summed over the entire FOV, for dsDNA, β-catenin, and CD56 as a function of acquisition time are shown. Right: Staining for dsDNA for a 150 μm × 150 μm inset for the first and last patients measured.

secondary ions generated by only 10 to 20 ns of sample sputtering. Consequently, ions are being generated for analysis less than 0.1% of the time, making the overall time needed to analyze the same amount of material by static SIMS three orders of magnitude longer over dynamic SIMS (23, 24).

With this in mind, we sought to design a purpose-built mass spectrometer for MIBI analysis that combines a high-resolution, continuous primary ion source with orthogonal acceleration TOF detection to achieve subcellular imaging that is both high throughput and highly multiplexed, without compromising sensitivity. Here, we describe MIBI-TOF, which enables routine, robust imaging of formalin-fixed paraffin-embedded (FFPE) human tissue biopsies with 36× greater throughput than our proof-of-principle work (4) while maintaining sensitivities comparable to magnetic sectors. MIBI-TOF can simultaneously quantify all naturally occurring elements from hydrogen to uranium. We used this capability here to simultaneously profile the subcellular expression and localization of 36 elementally labeled antibodies as well as native biological elements such as phosphate and iron. In addition, we show that MIBI-TOF allows repeat scanning of a single section, enabling intelligible study designs at different scales of throughput and resolution, or even acquisition of multiplexed three-dimensional images.

We leveraged these properties to reconcile inpatient heterogeneity of tumor and immune cell phenotypes. Heterogeneity in the phenotypes of tumor and stromal cells within lesions presents a major challenge for cancer therapy and is increasingly appreciated as a determinant of disease recurrence (25). In previous work, we used MIBI-TOF to characterize the tumor immune microenvironment in a cohort of 41 triple-negative breast cancer (TNBC) patients and found connections between the presence and organization of specific immune cell types and overall survival (26). However, the regional distribution of tumor and immune cell phenotypes remains unclear, as well as the generalizability to the entire tumor specimen of patterns identified from a single field of view (FOV) within a patient's cancer sample.

As an example of how multiplexed imaging can be used to resolve regional heterogeneity in the tumor immune microenvironment, we profiled the subcellular expression and localization of 36 proteins, including tumor and immune cell phenotypes as well as immunoregulatory proteins, in eight distinct regions from a single triple-negative breast tumor. We found heterogeneity in tumor cell phenotypes with a significant correlation to regional distribution. In contrast, immune phenotype and cellular composition were more structured across all regions and could be reconciled by a simple model of context-dependent recruitment of immune cells, similar to our previous observations across patients. Expression of specific immunoregulatory proteins, such as PD-1 and PD-L1, was restricted to specific immune cells in a well-defined spatial organization, where PD-L1⁺ myeloid-derived suppressor-like cells inhabit the tumor border, followed by a lymphocyte-rich zone. This organization persisted in different regions of the tumor, indicating robustness of the immune response, despite the heterogeneity in tumor phenotypes. Together, MIBI-TOF is uniquely positioned to examine numerous questions in the fields of cancer, immunology, and neurobiology in large clinical cohorts.

RESULTS

High-throughput, highly multiplexed tissue imaging

The design of MIBI-TOF focused on highly multiplexed mass detection, increased FOV size, and minimized image acquisition times

while maintaining high sensitivity. As shown in Fig. 1B, MIBI-TOF is composed of several key parts: a sample stage for microscope slides; a primary ion source and column for sputtering the specimen and generating secondary ions; a raster scanner, which sweeps the primary ion beam across the selected FOV in a stepwise pattern; an electrostatic analyzer (ESA), which filters secondary ions with respect to kinetic energy; and an orthogonal acceleration TOF mass spectrometer, which can discriminate and quantify elemental isotope abundance from the continuous introduction of ions. A detailed description of instrument specifications can be found in Materials and Methods.

To increase the FOV size and minimize image acquisition times compared to previous demonstrations (4), the primary ion source and column were configured to maximize sample sputtering while maintaining spot sizes suitable for subcellular tissue imaging (spot diameter, <1 μm). The larger FOV was achieved by increasing the working distance between the ion source and the sample from 400 μm on the NanoSIMS to 15 mm on MIBI-TOF. To reduce acquisition times under these conditions without compromising spatial resolution, we increased the current density (primary ion current/spot size) by using an O₂⁺ duoplasmatron ion source with 20× higher source brightness with a primary column operating at 30 kV acceleration voltage (compared to 16 kV shown previously) (4). This allowed us to increase the FOV area by over 60-fold compared with the NanoSIMS (1) (Fig. 1, C and D) while also increasing the current density sevenfold (at 200-nm spot size: MIBI-TOF has a current of 175 pA using O₂⁺ versus 25 pA using O⁺ for NanoSIMS; Fig. 1E). This configuration reduced the time required to scan a 100 μm × 100 μm FOV at 500-nm resolution from 17 to 3 min (Fig. 1, F and G). Furthermore, MIBI-TOF can collect data on up to 42 metal-labeled antibodies simultaneously, whereas the NanoSIMS can only monitor seven channels at a time (4). Together, these improvements reduce the acquisition time for 42 channels at these settings from 102 min by NanoSIMS to 3 min by MIBI-TOF, resulting in a 36-fold effective increase in throughput.

To acquire full elemental mass spectra from a continuous ion source, we replaced the magnetic sector with an orthogonal acceleration TOF analyzer with a high spectral scan rate (Fig. 1, B and H). Notably, unlike linear TOF analyzers typically used in static SIMS, orthogonal acceleration dictates the start time of each TOF spectrum independently of the incoming secondary ion flux. Limiting the mass range to 1 to 240 mass/charge ratio (m/z) permits a scan rate of 80 kHz such that 25% of all incoming ions at 150 m/z (60 eV ion energy) are orthogonally accelerated and quantified. Although magnetic sector instruments have high mass resolution and near absence of tailing of one mass peak into another (>10,000 $m/\Delta m$, >10⁻⁶ abundance sensitivity) (27, 28), these specifications far exceed what is needed to resolve and quantify nominally spaced elemental ions. Head-to-head comparisons using a molybdenum foil standard demonstrated MIBI-TOF to have sensitivities approaching magnetic sector instruments (MIBI-TOF ion transmission is 32% relative to NanoSIMS 50 L; Fig. 1I and fig. S1A) while still achieving the mass resolution sufficient for an elemental assay [1088 $m/\Delta m$ full width at half maximum (FWHM) at 98 m/z , 0.4% abundance sensitivity; Fig. 1, J and K, and fig. S1, A to C]. A detailed discussion of instrumental features that permit such high ion transmission can be found in Materials and Methods.

Although the TOF here can easily resolve elemental isotopic reporters, delineating them from interfering polyatomic ions with the same nominal mass can be more challenging. To reduce the contribution of interfering polyatomic ions (i.e., organic adducts, oxides,

and hydrides), we introduced an ESA, which acts as an energy filter on the secondary ions (Fig. 1, B and L). An extraction field directs the secondary ion flux containing monoatomic and polyatomic ions through the ESA, which has been tuned to preferentially transmit mono-atomic ions, which have a larger proportion of high-energy species relative to polyatomic ions (Fig. 1L and fig. S1D) (29). As a result, ~80% of mono-atomic elemental ions entering the ESA are transmitted to the entrance of the TOF, while the relative abundance of interfering polyatomic ions is attenuated nearly 10-fold (fig. S1, E and F).

Last, to increase compatibility with an anatomic pathology workflow, we used an airlock system for loading standard microscope slides that has reduced sample exchange times from 25 to 3 min (Fig. 1B; Materials and Methods). A detailed description of this subsystem can be found in Materials and Methods. This, combined with a novel method of conductive gold slide preparation (Materials and Methods), allows us to use conventional techniques for immunohistochemistry (IHC) using FFPE tissue sections (fig. S1G). As a demonstration of this, Fig. 1M depicts a 500 $\mu\text{m} \times 500 \mu\text{m}$ FOV multiplexed image of an archival human hippocampus with the hallmark curved dense nuclear band of the dentate gyrus (Fig. 1M, arrow), a particularly challenging case for multiplexed fluorescence imaging because of the high levels of autofluorescence arising from the tissue itself. This highly multiplexed subcellular analysis captures not only general neuro-anatomical features [double-stranded DNA (dsDNA), EIF4A2, CD289, NCAM/CD56, and myelin basic protein (MBP)] but also the identity and location of glial subpopulations [i.e., microglia (IBA1) and astrocytes (GFAP)] and specific neuronal (VGLUT2) populations.

In addition to charged secondary ions, primary beam rastering also produces secondary electrons that can be visualized with the system's secondary electron detector (SED image, Fig. 1N) using primary ion currents that remove negligible amounts of sample. The SED image delineates overall tissue architecture reminiscent of bright-field microscopy and can be used to visualize the sample in real time for direct FOV selection (frame rate: 1 to 4/s). Using this, hundreds of FOVs can be preselected and subsequently acquired in an automated fashion with no additional input. This allowed a continuous, 24-hour-a-day acquisition for 12 consecutive days, showing remarkable stability over time across distinct channels at distinct intensities ($-0.09 < R < 0.05$; Fig. 1O). Together, the combination of these features reinforces how MIBI-TOF can sensitively and robustly visualize the abundance and subcellular distribution of dozens of proteins simultaneously, and on time scale enabling large-scale studies.

Sensitive imaging across the elemental spectrum with a quantitative dynamic range of >100,000

To benchmark the effective sensitivity for detecting metal-tagged antibodies in tissue, we stained human FFPE tonsil sections with 16 different elemental reporter conjugates that were each generated using a single CD45 antibody clone (30, 31). For each section, we compared the number of metal atoms detected by MIBI-TOF per unit area to the absolute values for the same area using solution-phase elemental mass spectrometry (Materials and Methods). The mean ion yield was 0.003, indicating that ~1 in every 300 reporter atoms in the tissue sample could be detected, with the most sensitive element [indium (In)] being ~1:100. Assuming a labeling ratio of 100 reporter atoms per antibody probe using conventional labeling chemistry (31, 32), this would permit single-antibody detection in a highly multiplexed platform (Fig. 2A and table S1). This sensitivity is crucial for detecting low-abundant proteins, which may be present in just a few copies

per cell (33), and for accurate subcellular quantification of proteins. Figure 2A summarizes the relative sensitivity between elemental metal tags. Significantly, sensitivity of MIBI-TOF far exceeded that of the most sensitive element reported using mass cytometry (CyTOF, 159Tb) by up to 37-fold depending on the elemental tag used ($\mu = 15$, std. = 9). In these experiments, we also found that the relative yield of elemental adducts (hydrides, oxides, and hydroxides) rarely exceeded 10% of the corresponding elemental signal ($\mu = 5.6\%$, std. = 2.8%). A table summarizing elemental adducts can be found in fig. S1H.

To assess the capabilities of MIBI-TOF in an applied biological setting, we imaged a breast cancer tissue section stained with 36 antibodies (Fig. 2, B and C). Images for the entire 36-plex image are shown in fig. S2. Figure 2B depicts the mass spectrum, summed over the entire image, at various scales. Within the same image, we were able to quantify both metal-tagged antibodies and endogenous elements that varied in abundance by over six orders of magnitude. This combination of high sensitivity, high dynamic range, and low cross-talk permitted us to quantify low abundance markers such as FoxP3 even in the presence of high abundance signals such as dsDNA that exceed it in intensity by over three orders of magnitude (Fig. 2, C to E). Figure 2G shows additional examples of how simultaneous detection of both low and high abundance proteins reveals spatially organized immune regulatory populations in archival human FFPE breast cancer sections. For example, PD-1⁺ CD4⁺ T cells were colocalized with CD8⁺ T cells or PD-L1⁺ macrophages, while B cells were found to infiltrate the tumor bulk.

To systematically assess detection linearity as a function of ion count rate, a gallium arsenide standard was sputtered with primary ion currents ranging over four orders in magnitude (Material and Methods). This demonstrated a linear counting dynamic range exceeding five orders of magnitude before saturating the time-to-digital ion counting system (Fig. 2F). These data illustrate how MIBI-TOF circumvents the analytical limitations of immunofluorescence, resulting from channel cross-talk and autofluorescence, to permit detection of multiple proteins that vary greatly in abundance, even within the same pixel.

In addition to elemental reporter tags, MIBI-TOF can simultaneously quantify both heavier and lighter elements down to hydrogen. This capability can be used to great effect to quantify elemental components native to the tissue section itself. For example, we quantified ¹²C and ³¹P, common elemental components of biomolecules, to obtain images of general tissue structure and nuclear features, respectively (Fig. 3). We were also able to detect endogenous metals involved in native biological processes while simultaneously acquiring phenotypic information from a 36-plex antibody staining panel. For example, quantitation of ⁵⁶Fe in an FFPE spleen section revealed iron stores that correlated and subcellularly colocalized with specific CD68⁺ macrophage subsets with variable amounts of heme oxygenase-1, an enzyme involved in iron porphyrin catabolism (Pearson $r = 0.67$, $P < 10^{-246}$; fig. S3A) (34). In addition, heavy metal constituents of histopathological counterstains, such as uranyl acetate, can be used to delineate tissue structure in a manner that is independent of protein expression (Fig. 3). Together, these extend the capabilities of MIBI-TOF imaging beyond metal-labeled antibodies.

High-dimensional rescanning for custom tissue pathology workflows and production of three-dimensional images

One of the greatest utilities of bright-field microscopy is the ability to revisit the same FOV in a tissue section multiple times at different resolutions. Along these lines, a common approach in anatomic

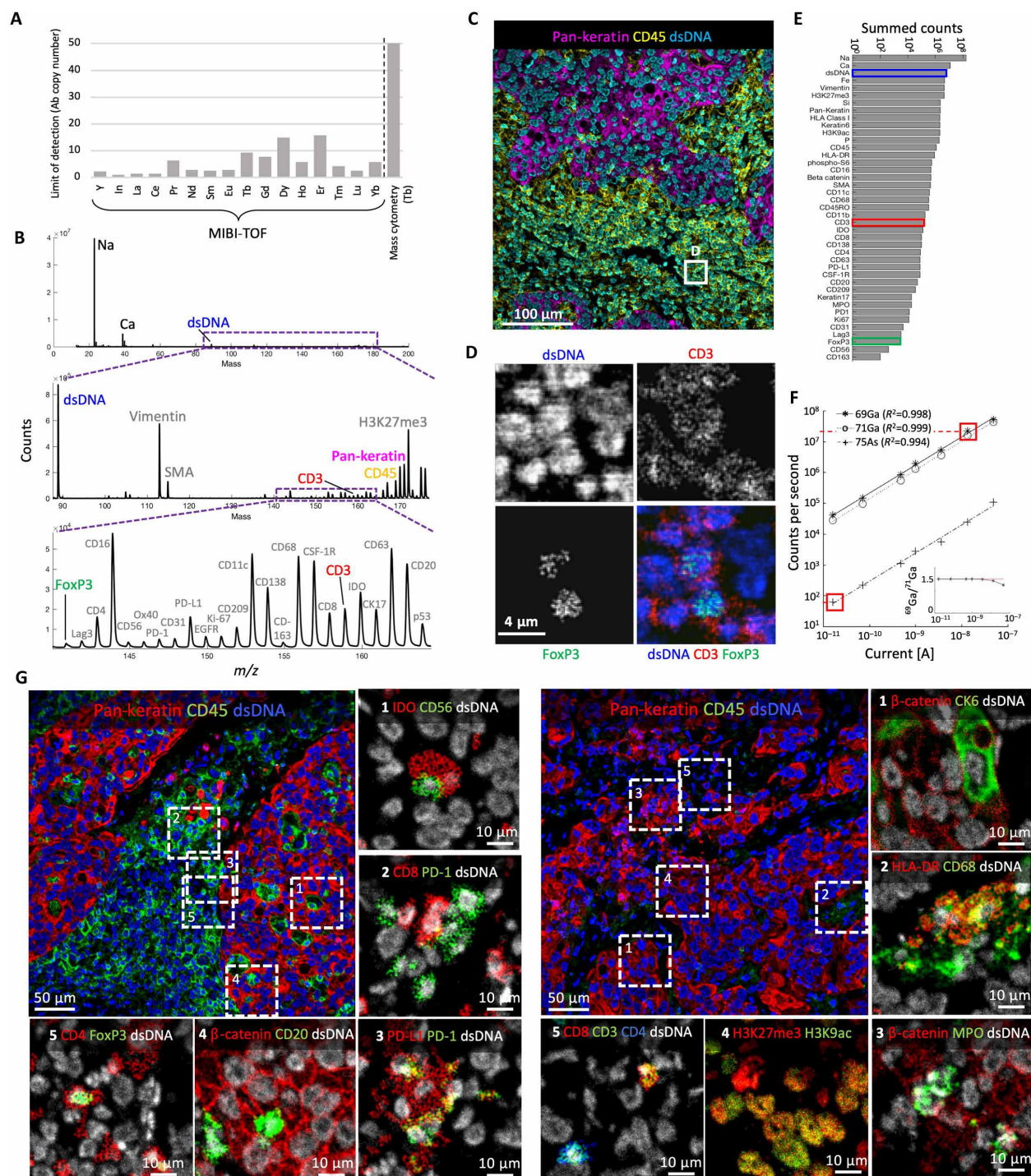


Fig. 2. MIBI-TOF can sensitively image across the elemental spectrum with a quantitative dynamic range of > 100,000. (A) Human FFPE tonsil sections were stained with a single CD45 antibody clone conjugated to 16 different elemental reporters, and the amount of metal detected by MIBI-TOF was assessed by comparing to values attained using normalized, solution-phase inductively coupled plasma mass spectrometry (ICP-MS). For each element, the number of antibodies needed for detection (assuming ~100 metals per antibody) is shown. The corresponding number is displayed for 159Tb, the most sensitive channel on CyTOF, which is, on average, 15-fold less sensitive. (B and C) FFPE human breast carcinoma was stained with a panel of 36 antibodies, and a 500 μm × 500 μm FOV was imaged by MIBI-TOF. (B) Mass spectrum, summed over the entire image, at various scales. (C) Multiplexed staining for dsDNA, pan-keratin, and CD45, corresponding to the spectrum in (B). White box marks inset shown in (D). (D) Zoom-in on (C), depicting staining for dsDNA, CD3, and FoxP3, ranging over three orders of magnitude in intensity. (E) For all channels, their intensities, summed over all pixels in the image from (C), over five orders of magnitude, are shown. (F) Measurements of counts per second for a gallium arsenate probe (y axis) for a range of extraction currents (x axis). Red boxes denote limits of linear range, which spans five orders of magnitude. Inset: Gallium isotopic ratio (⁶⁹Ga/⁷¹Ga) measured by MIBI-TOF (black) matches the known ratio (1.5, red) and is constant over three orders of magnitude before saturating the counts system. (G) FFPE human breast carcinoma was stained with the same panel as in (B) and two 500 μm × 500 μm FOVs were imaged by MIBI-TOF. Top left image depicts the entire region. Surrounding images highlight expression of distinct markers in specific regions.

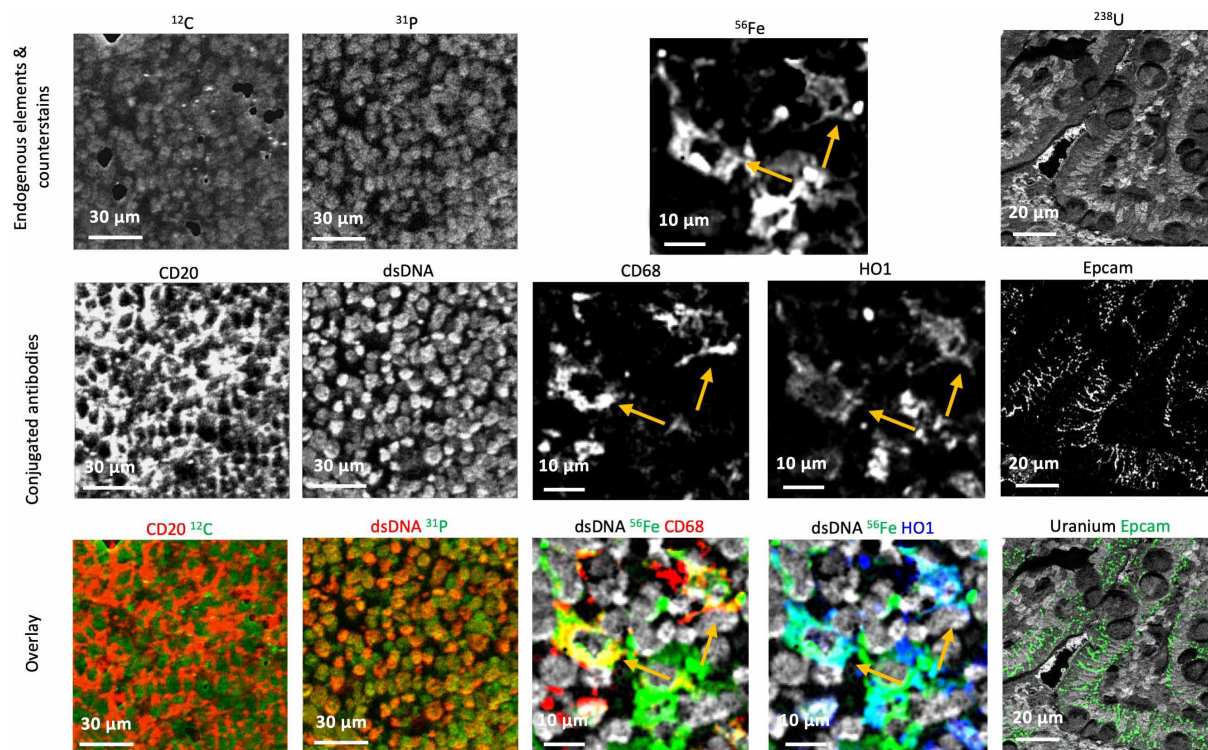


Fig. 3. MIBI-TOF enables imaging of metal-tagged antibodies simultaneously with histochemical stains and endogenous biological elements. Tissue sections from tonsil (left), spleen (center), and GI (right) depicting simultaneous measurements of natural elements (^{12}C , ^{31}P , and ^{56}Fe), metal-tagged antibodies (CD20, dsDNA, CD68, HO1, and Epcam), and counterstains (uranyl acetate). Arrows denote CD68⁺ HO1⁺ macrophages with high ^{56}Fe .

pathology is to first examine a large area at low magnification to identify regions of interest to inspect in greater detail at higher magnification. However, virtually all previously reported multiplexed imaging platforms that use cyclic fluorescence imaging or laser ablation mass spectrometry can only image a given area once, prohibiting this type of iterative workflow.

To achieve this bright-field microscopy-like utility, we designed the platform such that the same area could be scanned multiple times, except now in multidimensional space. Here, with each scan, secondary ions are released in proportion to the ion dose delivered to the sample per unit area ($[\text{primary current}] \times [\text{acquisition time}] / [\text{FOV area}]$). Because the primary current can be instantly and accurately adjusted across a $10,000\times$ range, a given FOV can be imaged with an initial low-resolution scan, followed by a subsequent high-resolution scan, by modulating the primary ion current (23). For example, MIBI-TOF imaging of a $200\text{ }\mu\text{m} \times 200\text{ }\mu\text{m}$ FOV of melanoma at $1\text{-}\mu\text{m}$ resolution was sufficient to resolve individual nuclei and took only 16 s (Fig. 4, A to C, survey scan, blue). Rescanning of the field using the same ion dose at 385-nm resolution revealed structural features of the nuclear envelope but increased the acquisition time to 17 min (Fig. 4, A to C, medium-resolution scan, orange). Increasing the resolution even further is possible (Fig. 4, A to C, high-resolution scan, 260 nm , red) and is accompanied by further increases in scan time. These data highlight an important advantage of ion beam sputtering: The system's sensitivity to metal-tagged reporter elements permits generation of robust images for most antigens using a fraction (5 to 10%) of the total bulk of a standard $4\text{-}\mu\text{m}$ -thick FFPE section. Thus, although each scan removes the biological material that has been imaged, high-dimensional images can be acquired under con-

ditions that leave much of the sample intact for additional scanning as described above or for other downstream ancillary studies such as laser capture microdissection (35).

Scan times at a given resolution scale linearly with FOV area, so an alternative way to reduce acquisition times is to reduce the overall FOV size. For example, a reduction of the FOV size from $200\text{ }\mu\text{m} \times 200\text{ }\mu\text{m}$ to $100\text{ }\mu\text{m} \times 100\text{ }\mu\text{m}$ while keeping the resolution fixed reduces acquisition times by fourfold. Last, depending on the abundances of the antigens being detected, the ion dose can be adjusted to ensure that a sufficient amount of material is analyzed (fig. S3, B and C). Thus, MIBI-TOF can be easily configured for a variety of applications, depending on the number of FOVs, FOV size, protein expression levels and resolution required for each particular study, and the time frame available for data collection.

Unlike chromophores and fluorescent molecules, the stable nature of elemental isotopic reporters in archival samples permits valid analysis even after extensive periods of time from the initial staining. Figure 4D shows serial sections of three breast carcinomas stained on May 2017. The first set of serial sections was analyzed days after staining, while the second set was stored at ambient temperature in room air for 1 year before analysis. When comparing the freshly stained and acquired versus stained and aged samples, we observe high correlations between the fresh and aged samples (e.g., Pearson $r = 0.95$, $P < 10^{-45}$ for CD20; Fig. 4E and fig. S3, D to F). Together, long-term sample stability and rescanning uniquely allows MIBI-TOF to recapitulate routine clinical and research procedures, all while gathering high-dimensional data that permit a detailed view of the tissue.

Last, by leveraging the precision of ion beam sputtering combined with the ability to rescan a field at a fixed resolution, we can also use

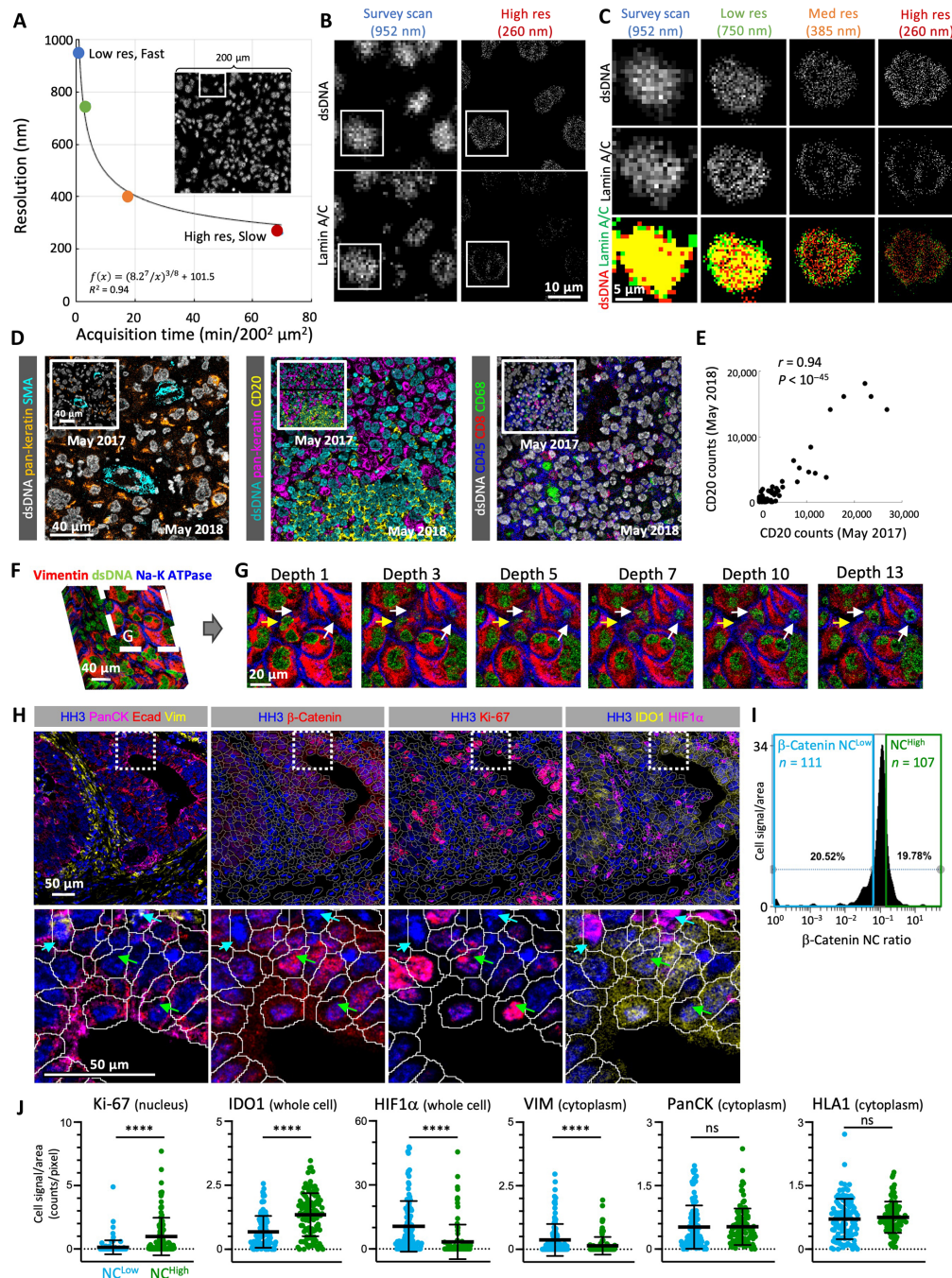


Fig. 4. MIBI-TOF enables multiscale, high-dimensional rescanning for customizable tissue pathology workflows and three-dimensional tissue reconstruction.

(A) A 200 $\mu\text{m} \times 200 \mu\text{m}$ melanoma biopsy (inset) was scanned four times at resolutions ranging from 260 to 1000 nm (y axis). The scan times for the different resolutions are shown (x axis). (B) Zoom-in on the inset in (A), showing staining for dsDNA (top) or lamin A/C (bottom) for the survey scan (left) and high-resolution scan (right). (C) Zoom-in on the inset in (B), showing staining for dsDNA (top) or lamin A/C (middle), and their overlay (bottom) for the different scans. Increasing detail of lamin A/C becomes available at higher resolutions. (D) Three FFPE breast carcinomas were stained with a 36-plex panel in May 2017, and 1-mm cores were visualized by MIBI-TOF days after staining (insets), or a year later (large images), with negligible deterioration in signal. (E) Second FOV from (D) was divided into a 10×10 grid. CD20 counts for each of the resulting 100 tiles in the images from 2017 (x axis) and 2018 (y axis) are shown. (F) Three-dimensional reconstruction of a 15-layer depth profile of archival 4- μm -thick FFPE melanoma tissue stained with a 20-plex panel. (G) Snapshots of selected depths. White and yellow arrows denote nuclei (dsDNA, green) that either appear or disappear, respectively, with depth, with corresponding disappearance or appearance of cytosol (vimentin, red) and membrane (Na-K ATPase, blue). (H) Images showing select marker expression in a colorectal tumor stained with a 34-plex panel. HH3, histone H3; PanCK, pan-keratin; Ecad, E-cadherin; Vim, vimentin. A select area is expanded in the bottom row, with cell segmentation outlines overlaid. Green and cyan arrows mark cells with high and low NC ratios of β -catenin, respectively. (I) NC ratio of β -catenin was calculated in all β -catenin⁺ tumor cells (PanCK⁺ or ECAD⁺). Cells within the highest and lowest quintile of β -catenin NC values were gated. (J) Expression of Ki-67, IDO1, HIF1 α , VIM, PanCK, and HLA1 was compared between β -catenin NC^{hi} and NC^{low} tumor cells in vertical scatterplots. Asterisks denote significant differences in mean cell signal intensity in the populations, **** $P < 0.0001$; ns, not significant.

MIBI-TOF analysis to derive three-dimensional spatial information. Each scan removes the uppermost portion of the tissue to reveal a deeper layer of the tissue bulk that is subsequently analyzed and removed in the following scan. Figure 4 (F and G) illustrates a 15-depth run on an archival 4- μm -thick FFPE tissue section of melanoma, resulting in ~ 250 -nm resolution in the Z dimension. Melanoma tumor nuclei (dsDNA, green) can be seen becoming more or less prominent in reciprocal fashion with the absence and presence of cytoplasmic (vimentin, red) and membranous proteins (Na-K ATPase, blue) (Fig. 4G, arrows, and movie S1). We also demonstrate the utility of Z-scanning to identify intranuclear areas with different ratios of H3K9 acetylation and H3K27 trimethylation (fig. S3, G and H), consistent with previous reports about epigenetic compartmentalization of epigenetic markers within interphase nuclei (36). This type of analysis lays the groundwork for three-dimensional reconstruction of archival tissues and should prove essential for areas of investigation not well suited to planar analysis such as neurobiology and gut immunology.

To demonstrate the utility of high-resolution scans, we explored the subcellular localization of β -catenin in human colorectal cancer (CRC). In CRC, adenomatous polyposis coli (APC) and β -catenin are commonly mutated, impairing APC-mediated proteasomal degradation of β -catenin and leading to its accumulation in the tumor cell cytosol and occasionally in tumor cell nuclei. Nuclear β -catenin has been shown to correlate with tumor progression, metastasis, and poor overall survival (37–39). Here, we profiled a $400\ \mu\text{m} \times 400\ \mu\text{m}$ FOV of CRC using MIBI-TOF with a panel of 34 proteins (table S3), including β -catenin (Fig. 4H, top row). We identified tumor cells that are positive for β -catenin and demonstrate the utility of MIBI-TOF to quantify the nuclear versus cytoplasmic levels (NC ratio) of this protein (Fig. 4I). Consistent with the literature, we found that, in some cells, β -catenin is predominantly localized in the nucleus and in others in the cytoplasm (Fig. 4H, bottom row, green and blue arrows, respectively). To explore how these variations relate to known canonical signaling pathways, we examined protein expression in the 20% of cells with the highest and lowest NC ratios ($n = 109$ and 115 cells, respectively). We found that cells with high NC ratios of β -catenin were more proliferative (Ki-67^+) and expressed more of the immune regulatory enzyme IDO1, whereas cells with the lowest NC ratios expressed higher nuclear levels of HIF1 α and intracellular vimentin ($P < 0.0001$; Fig. 4J). These observations are consistent with the known output of the β -catenin/T cell factor (TCF)/lymphoid enhancer factor (LEF) transcriptional program, which, when in the nucleus, up-regulates IDO1 (40) and promotes cell cycle progression (41). In hypoxic tumor cells, however, HIF1 α competes with TCF for β -catenin binding and abrogates this cell cycle promotion (42). This is known to drive epithelial-to-mesenchymal transition genes, including vimentin (43).

Together, we leverage the multiplexed, quantitative, high-resolution imaging of MIBI-TOF to show that tumor cells with different NC ratios of β -catenin occupy distinct functional states. From a single image derived from a primary patient tumor, these findings offer insight into the role of β -catenin subcellular localization and its association with poor patient outcome implicated by a more proliferative, immunosuppressant, and pro-tumorigenic state.

MIBI-TOF reveals a regional tumor phenotype bias contrasting a structured immune response

Harnessing the utility of all the features described above, we used MIBI-TOF to study the intratumor heterogeneity of both tumor and immune cell types in situ. To this end, we stained a full archival TNBC

tissue section ($0.8\ \text{cm} \times 1.04\ \text{cm}$) with an antibody panel for interrogating 36 proteins of the tumor-immune microenvironment that has been previously applied to study tissue cores from a cohort of 41 TNBC patients (26). The panel included tumor-related proteins (e.g., cytokeratins), functional markers for proliferation and metabolic activity (e.g., Ki-67 and pS6), immune-related proteins (e.g., CD4 and FoxP3), and four immunoregulatory proteins (PD-1, PD-L1, LAG3, and IDO) currently targeted in the clinic or undergoing immunotherapy drug trials. We first performed a 36-plex survey scan of the full tissue section at $1.5\text{-}\mu\text{m}$ resolution by automated tiling of 520 separate $400\ \mu\text{m} \times 400\ \mu\text{m}$ FOVs (Fig. 5, A and B).

Following the survey scan, we randomly chose eight $400\ \mu\text{m} \times 400\ \mu\text{m}$ regions for subsequent rescanning at a resolution of $500\ \text{nm}$ (Fig. 5, A and B), obtaining information on both protein expression patterns and spatial localization of 11,120 cells. Regions were selected and then acquired in a single run to reduce technical variability. Images were processed together by a custom computational pipeline, which included denoising and cell segmentation (Materials and Methods) (26). The raw and processed data, as well as the segmentation masks, can be accessed through a web interface and downloaded at <https://mibi-share.ionpath.com>. Visual inspection demonstrated regional variations in expression of various proteins by the tumor cells, such as CK17, Ki-67, and HLA-DR (Fig. 5C).

To systematically identify tumor phenotypes, we performed clustering analysis (44) of tumor cells across all regions. The analysis revealed 10 tumor phenotypes, as defined by combinatorial expression of epidermal growth factor receptor (EGFR), Ki-67, HLA-DR, cytokeratin 6 (CK6), CK17, and PanCK (Fig. 5D). Distinct tumor phenotypes were disproportionally represented in distinct regions of the tumor and clustered by region (Fig. 5, C to F). For example, regions 7 and 8 were characterized by positivity of HLA-DR on all tumor cells and a high proliferation rate, as gauged by nuclear expression of Ki-67. On the other hand, regions 3 and 6 were characterized by no expression of HLA-DR on tumor cells, low proliferation rate, as gauged by expression of Ki-67, and positive expression of cytokeratins (Fig. 5G). This regional distribution of tumor phenotypes persists across length scales, as demonstrated by the correlation between the expression patterns of tumor cells in different regions and the physical distance between these regions (Pearson $r = -0.69$, $P < 10^{-5}$; Fig. 5H). We validated that the regional clustering of tumor phenotypes is not likely attributable to random sampling. To this end, we compared the observed distributions of phenotypes in different regions to that expected from a simple Poisson distribution and found significant deviations for most tumor phenotypes [false discovery rate (FDR)-corrected Kolmogorov-Smirnov across all tumor and immune phenotypes: $q = 0.0004$ for $\text{CK}^+ \text{Ki-67}^+$ and $q = 0.005$ for $\text{CK}^+ \text{HLA-DR}^+ \text{Ki-67}^+$; Fig. 5I and fig. S4A]. Together, we find a large degree of variation in tumor phenotypes, as previously observed (2, 25), and show that these phenotypes are preferentially localized to distinct regions of the tumor, which may play an important role in the tumor ecosystem and relate to the dynamics of clonal evolution.

To round out our assessment of tumor microenvironment heterogeneity, we next evaluated the composition and regional distribution of immune cell phenotypes. We clustered immune cells into 11 groups based on the expression of 11 proteins (CD3, CD4, CD8, CD11b, CD11c, CD16, CD20, CD45, CD56, CD68, and FoxP3) (Fig. 6A). Unlike tumor cells, immune cells clustered by expression, regardless of the region in which they were located (Fig. 6, B to D). An exception to this was the enriched presence of neutrophils in

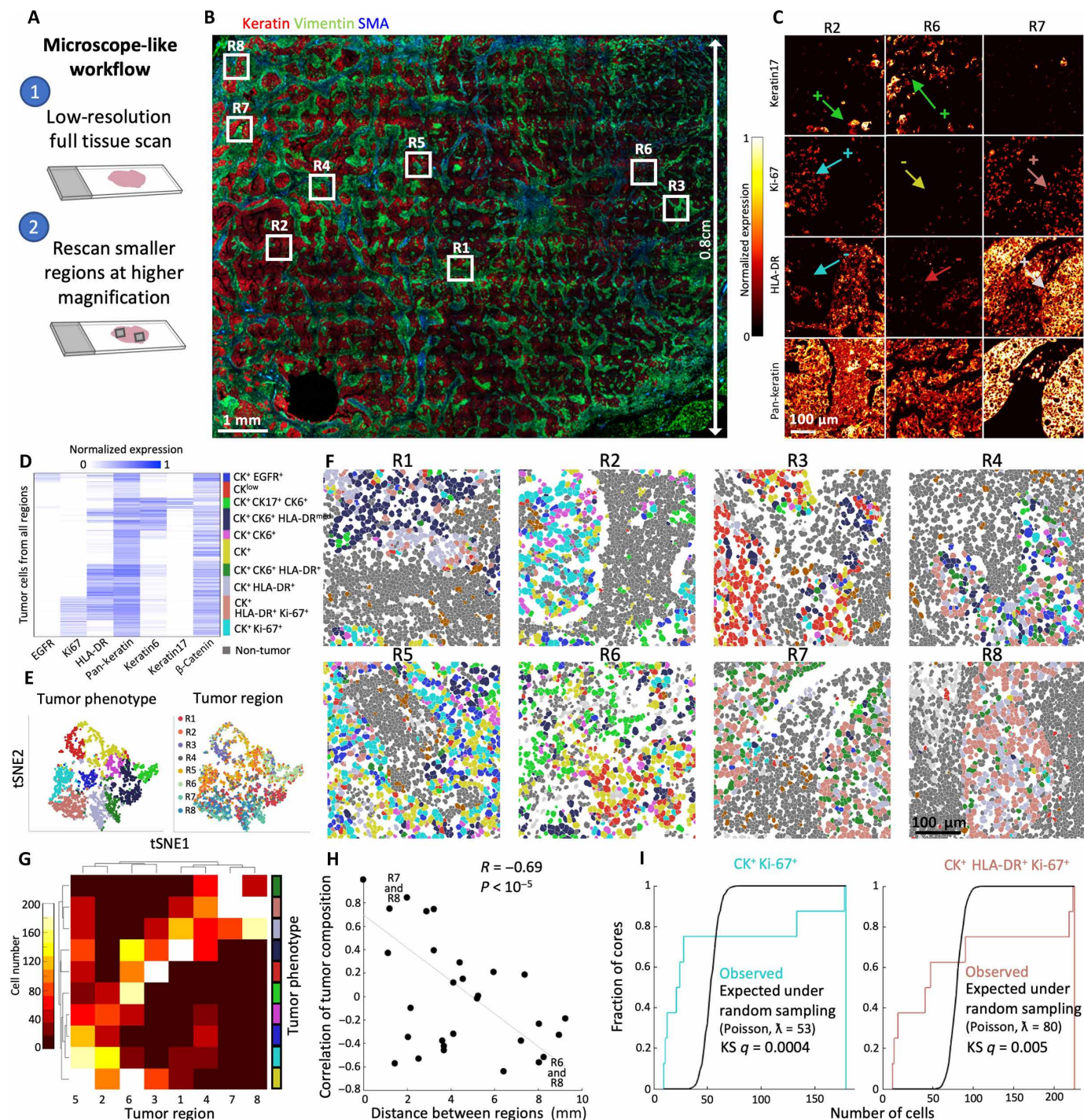


Fig. 5. Intrapatient heterogeneity in tumor phenotypes is associated with spatial location. (A) Diagram of microscope-like analytical workflow, enabled by MIBI-TOF. (B) Archival breast cancer tissue section was stained with 36 antibodies, and a 0.8 cm \times 1.04 cm FOV was visualized using MIBI-TOF at 1.5- μ m resolution. The full image was constructed from 520 400- μ m FOVs, tiled 26 \times 20. Eight regions (white squares) were subsequently rescanned at 500-nm resolution. (C) Expression of four proteins across three regions shows regional heterogeneity in expression. Colored arrows mark cells belonging to specific tumor clusters in (D). (D) Tumor cells from all regions were clustered by protein expression. Expression values for each protein are scaled from zero to one. (E) tSNE embedding for tumor cells. Cells are colored by either phenotype as in (D) (left) or region (right). (F) Pseudo-coloring of all regions. Tumor cells are color-coded as in (D). Other cell types are colored gray. (G) For each tumor region (x axis), the number of cells from each tumor phenotype is shown (y axis). (H) Pearson correlations of pairwise comparisons of tumor cell composition in different regions (y axis) are shown as a function of the distance between the regions (x axis). Overall correlation indicates that close regions are more similar in composition of tumor phenotypes. (I) Cumulative distribution functions depicting the fraction of cores (y axis) with up to a number of cells from a given tumor phenotype (x axis) for the CK⁺ Ki-67⁺ phenotype (left) and CK⁺ HLA-DR⁺ Ki-67⁺ phenotype (right). Observed distributions (cyan and pink, respectively) are compared with the Poisson distribution expected from random sampling using the Kolmogorov-Smirnov statistic and FDR-corrected for multiple hypothesis testing across all tumor and immune phenotypes.

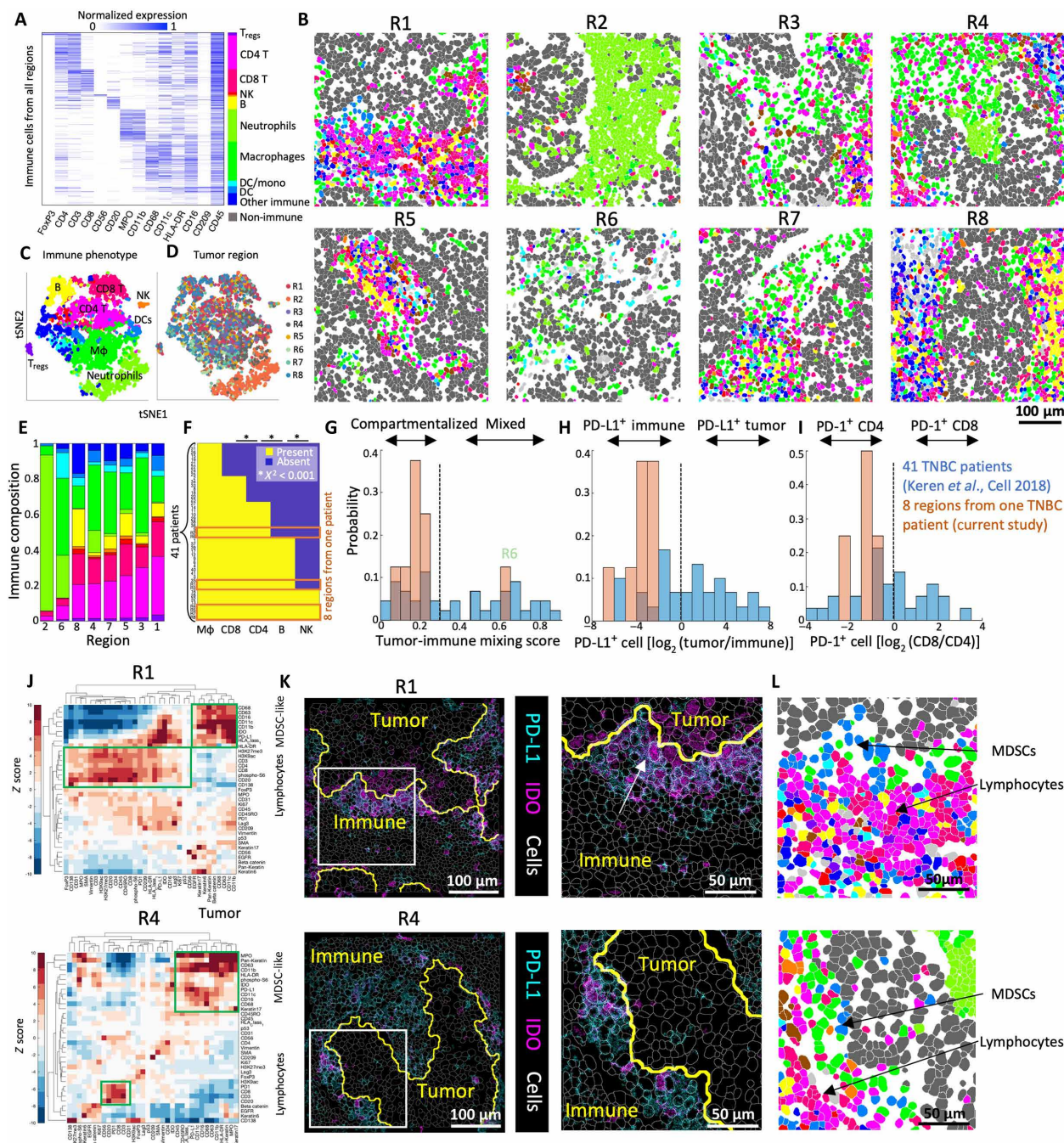


Fig. 6. Structured immune composition and organization across tumor regions. (A) Immune cells from all regions were clustered by protein expression. Expression values for each protein are scaled from zero to one. (B) Pseudo-coloring of all regions. Immune cells are color-coded as in (A). Other cell types are colored gray. (C and D) tSNE embedding for immune cells. Cells are colored by either immune lineage (C) or region (D). (E) Immune composition normalized from zero to one (y axis) in all regions (x axis). Regions are ordered by percentage of CD4⁺ T cells (magenta). (F) For five immune populations (x axis), their presence or absence across a cohort of 41 TNBC patients (26) (y axis, patients numbered 1 to 41) and in the eight regions from a single patient depicted in this study (orange rectangles, R1 to R8) is shown. (G) Tumor-immune mixing scores were calculated for a cohort of 41 TNBC patients and the eight regions from a single patient depicted in this study. The probability density function of tumor-immune mixing across patients (blue) and across regions (orange) is shown. Seven of eight regions are defined as compartmentalized, according to a previously defined threshold (26). (H) Same as (G), for the log ratio of PD-L1⁺ tumor and immune cells. In all regions, PD-L1 is expressed predominantly on immune cells. (I) Same as (G), for the log ratio of PD-1⁺CD8⁺ and PD-1⁺CD4⁺ T cells. In all regions, PD-1 is expressed predominantly on CD4⁺ T cells. (J) Heatmaps depicting spatial enrichment z scores between pairs of proteins in regions R1 (top) and R4 (bottom). Green squares denote enriched spatial proximity of myeloid-derived suppressor-like cells (MDSC-like) near the tumor and of lymphocyte-rich regions. (K) Left: Color overlays of PD-L1 (cyan), IDO (magenta), and cell segmentation (white) in regions R1 (top) and R4 (bottom). Tumor-immune border as identified by an automatic pipeline is highlighted in yellow. Right: Zoom-in on boxed region in left panel. Immunoregulatory proteins PD-L1 and IDO are predominantly expressed by immune cells close to the tumor-immune border. (L) Pseudo-coloring of immune cells as in (B) for the zoomed-in regions in (K), showing a concentric organization of tumor cells, surrounded by MDSC-like and then lymphocyte-rich regions.

region 2 (Fig. 6D), possibly indicating local inflammation. Immune composition across regions was more conserved than tumor composition across regions, where many differences in immune cell types here could be attributed to random sampling (fig. S4A).

We previously analyzed the immune composition in a cohort of 41 TNBC patients, where we suggested that sequential recruitment of specific immune populations into the tumor site could explain the observed patterns of immune cells across patients (26). We therefore asked whether the observed changes in immune cell type composition across regions within a single tumor could be attributed to different stages of infiltration, similar to observations across patients. To this end, for each tumor region, we classified the different immune populations that were identified to co-occur in the previous study as either present or absent in the sample. We then integrated the results from both studies and clustered the resulting dataset (Fig. 6, E and F). We found that results from different tumor regions from a single patient here coincided with our previous observations, with a notable interdependence between the presence and absence of individual immune populations. For example, all regions that had B cells also had CD4⁺ T cells and CD8⁺ T cells (χ^2 test: $P = 6.5 \times 10^{-6}$ and $P = 0.002$, respectively). All regions that had natural killer (NK) cells also had B cells ($P = 7.5 \times 10^{-4}$). These results extend our previous model whereby specific immune cells are recruited to the tumor site in a context-dependent manner. While it reinforces a structured ruleset for immune cell infiltration, it now suggests that the overall progression of this process can be variable across distinct tumor regions.

Next, we evaluated the spatial organization of tumor-infiltrating immune cells and the expression patterns of immunoregulatory proteins by distinct immune cell populations. It has been established that TNBC tumors can be classified as “cold,” with low immune infiltration, and “hot,” with high immune infiltrate, and that this property is correlated with overall survival (45–48). Our previous work demonstrated that within the hot tumors, there were two categories based on cellular organization: mixed, with high spatial mixing between tumor and immune cells, and compartmentalized, in which there are regions composed predominantly of one cell type or the other (26). We further demonstrated that these histological organizations were associated with expression of immunoregulatory proteins by specific immune/tumor cell types in defined locations. As such, mixed tumors were associated with expression of PD-L1 on tumor cells and PD-1 on CD8⁺ T cells, whereas compartmentalized tumors tended to have PD-L1 expression on myeloid-derived cells at the tumor-immune boundary and PD-1 expression on CD4⁺ T cells and were associated with improved survival. While this ruleset was established across 40+ patients with prognostic value, these attributes have not been examined for variability across tumor regions. Here, for each region, we calculated a mixing score between tumor and immune cells, as previously described (26), and compared the distribution of mixing scores in different regions of a single patient to the distribution of mixing scores from different patients. We found that the mixing scores calculated for different regions of a single tumor spanned a narrow range relative to the mixing scores from different patients and that seven of eight regions indicated that this was a compartmentalized tumor according to our previously defined threshold (Fig. 6G). Similarly, we evaluated the expression of PD-L1 on tumor and immune cells and the expression of PD-1 in CD4⁺ and CD8⁺ T cells in different tumor regions and compared it to observations across different patients. As expected from the mixing score, the predominant expression of PD-L1 was on immune cells and PD-1 on CD4⁺

T cells in all eight regions, consistent with a compartmentalized histological organization (Fig. 6, H and I). Together, these data, which connect tumor-immune organization and immunoregulatory protein expression, coincide with observations from our 41-patient TNBC study. They further suggest a cohesiveness of the immune response across tumor regions, despite regional heterogeneity in tumor phenotypes.

Last, we evaluated the spatial organization of the tumor-immune landscape in TNBC by assessing enrichment in spatial proximity for pairs of markers in this compartmentalized TNBC tumor (Fig. 6J), as previously described (26). For each pairwise comparison, we randomized the location of positive cells while keeping their numbers constant to generate an expected distribution of distances and then calculated a *z* score for the observed value in the tissue, indicating enrichment for spatial proximity. As with the other immune features, we found similarities in organization between distinct tumor regions. Specifically, we identified myeloid cells positive for the immunoregulatory proteins PD-L1 and IDO next to tumor cells, as well as a cluster of lymphocytes (Fig. 6J). This concentric organization, whereby the tumor-immune border is lined with myeloid-derived suppressor-like cells, followed by a layer of lymphocytes, is shared across regions regardless of heterogeneity in tumor phenotypes (Fig. 6, K and L) and recapitulates our previous observations across patients (26).

Together, we harnessed MIBI-TOF's capabilities for sensitive, fast, highly multiplexed imaging of large FOVs and rescanning at varying resolutions to provide an example of how we can interrogate the regional intratumor heterogeneity in TNBC in a single patient and reconciled it to observations from small areas sampled from a large patient cohort. For this patient, we found substantial regional heterogeneity in tumor phenotypes accompanied by a structured immune response. Differences in the abundance and composition of immune cell types across regions were well explained by our previous model, whereby specific immune cells may be recruited to the tumor site in an ordered manner. This suggests that local variation in immune cell population could be explained by a conserved ruleset for recruitment to the tumor. Further, immune phenotypes, including cell type-specific expression of checkpoint proteins, and their histological organization within the tumor microenvironment were highly conserved across regions. Specifically, we identify a cross-regional concentric organization pattern, whereby the tumor regions are surrounded by myeloid-derived suppressor-like cells, which are further surrounded by lymphocyte-rich regions. Together, the regional intrapatient heterogeneity in immune composition and organization agrees with the trends that we have previously observed across patients but lies in a smaller, more confined phenotypic space. While this analysis should be performed for additional patients, it suggests that although the immune system is exposed to many different tumor-related phenotypes, it integrates them into a more restricted set of outputs. Thus, understanding immune organization could provide a promising avenue for reducing the complexity of tumor classification with potential benefits for patient stratification.

DISCUSSION

MIBI-TOF is a versatile platform for high-dimensional imaging using standard archival FFPE tissue and conventional IHC workflows. Beyond multiplexing, the imaging analysis is sensitive and modular, which enables detection of low-abundant antigens at high spatial resolutions. Up to 42 elemental reporters can be used currently, and throughput has been increased by 36-fold over our previous work

(4). The system is designed to facilitate common clinical workflows, including imaging of a sample at different resolutions, and decoupling of the staining and imaging processes, which allow to revisit a sample after prolonged periods of time.

In addition to antibody-based approaches, elemental labeling of nucleic acid derivatives should extend the platform to DNA and RNA in situ hybridization (ISH). Given that the feasibility of adapting fluorescence-based ISH probes to elemental reporter assays has been demonstrated previously (49, 50), we expect to implement these capabilities in the near future, allowing single-cell quantitation of both genomic copy number variants and transcript enumeration within a native histological context.

With a mass range of 1 to 240 m/z , MIBI-TOF can also quantify numerous endogenous elements including carbon, phosphorous, iron, and calcium. The spatial distribution of endogenous biological elements can be used for cellular segmentation to relate the abundance of enzyme-coordinated metal cofactors to single-cell phenotypes or to assist in identifying abnormal regions of tissue, such as necrosis or fibrosis. Notably, we are working to extend MIBI-TOF to simultaneously detect ^2H and ^{13}C heavy isotope reporters, which can be used to covalently label the protein or DNA of cells expanded *ex vivo*. Because these isotope reporters are relatively inert, this capability is particularly applicable to ongoing clinical trials using engineered T cell therapies, allowing the assessment of how transplanted cell phenotypes evolve over time.

The future of MIBI-TOF applications will be further accelerated as brighter primary ion sources are implemented with up to 20 times the current density as those used here. These improvements should reduce acquisition times proportionally such that sample throughput would be rapid enough to permit turnaround times compatible with routine anatomic pathology. In addition, the higher milling rates achieved with these ion sources will also permit rapid depth profiling of large samples such that high-throughput three-dimensional rendering of tissue architecture would be feasible on a large scale. Full utilization of these capabilities will require development of purpose-built computational tools for image segmentation, annotation, visualization, and feature extraction, which we expect to be an important avenue of future research. Along with deployment of the necessary instrumentation, we are working to implement and distribute our initial versions of these tools to enable broader use by clinical and basic research scientists. Together, MIBI-TOF represents a robust platform to help overcome long-lasting analytical challenges in systems biology and could play a key role in many important discoveries in cancer biology, immunology, neuropathology, and beyond.

MATERIALS AND METHODS

MIBI-TOF tissue analyzer

The MIBI-TOF tissue analyzer is a dynamic SIMS instrument with orthogonal time of flight ion detection (Fig. 1B). The instrument is equipped with a duoplasmatron O_2^+ ion source coupled to a 30-kV primary ion column (IOG 30D, Ionoptika, Eastleigh, UK) operating in crossover mode at a working distance of 15 mm and 45° incident angle to the sample stage. The primary column is a conventional two-lens design, where the first lens (L1) demagnifies the virtual source and the second lens (L2) functions as a probe-forming objective. Depending on the acquisition time and image resolution desired for a specific experiment, L1 voltages of 17 to 26 kV were used to achieve primary current and spot sizes of 18 nA and 1 μm to 240 pA and 230 nm, respectively.

Tissue sections were loaded into the vacuum chamber using a custom-designed sample carrier that can accommodate two standard microscope slides. The sample loading mechanism is an airlock composed of an automated compressible o-ring seal driven by a DC motor. During a sample exchange, the motorized stage carrying the sample holder exits the analysis chamber and moves to a point directly under the sample exchange port. A gear-driven airlock is activated and lowered by the DC motor onto the outer edges of the circular sample stage such that a compression seal is formed with the outer edges. The sample holder containing the microscope slides is now isolated from the vacuum chamber. This isolated compartment is vented to atmospheric pressure. After the samples have been loaded, the vented compartment is pumped via an independent turbo. After this pumping period, the DC motor raises the airlock and the stage reenters the analysis chamber. Sample loading times are approximately 3 min, while the analysis chamber typically reaches its operational base pressure of 5×10^{-7} within 6 min.

Course navigation of tissue sections was achieved via a point and click interface using a co-registered photo of the sample stage. Final FOV selection was performed using an SED (SED 03, Ionoptika, Eastleigh, UK), which allows real-time imaging of the sample surface as the primary ion source rasters the sample using a primary ion current between 500 pA and 1 nA. Lateral stage coordinates for each FOV specified by the user were tabulated in the acquisition software, and imaging run parameters were specified. Before starting each run, the primary ion imaging system was focused on a test region of the sample of interest by adjusting the L2 voltage while imaging in real-time SED mode. A stigmator octopole within the primary ion column was also adjusted to minimize discernible astigmatism. A description of key acquisition parameters and their adjustable ranges of values are as follows: primary ion current, 1 pA to 1 μA ; FOV size, 10 $\mu\text{m} \times 10 \mu\text{m}$ to 1 mm \times 1 mm; pixel dwell time, >100 μs ; number of pixels: 128 \times 128 to 2048 \times 2048; number of depths: one or more; mass range, up to 240 m/z .

Specific settings for each experiment are denoted in table S2. For each pixel in the image, corresponding positions on the tissue were sequentially sputtered with the primary ion beam using a fly back raster pattern (IGM 300, Ionoptika, Eastleigh, UK). Secondary ions were collected using a relatively modest extraction field of approximately 60 V/mm, which yielded an optical gate of approximately 800 μm with the use of dynamic emittance matching (DEM). Secondary ions subsequently pass through a 90° ESA operating in a non-dispersive configuration with 20-eV energy acceptance that has been tuned for preferential transmission of monoatomic (elemental) ions relative to polyatomic organic species. The ions then enter an orthogonal time-of-flight mass spectrometer with a median energy acceptance of 65 eV, mass range of 1 to 240 m/z , and mass resolution of 1088 $m/\Delta m$ (FWHM at 98 m/z) operating at 80-kHz repetition rate (fig. S1). Under these conditions, the predicted TOF transmission of ions with 65 eV median energy and 150 m/z is 25%. A discrete dynode ion detector (MagneTOF, ETP Electron Multipliers, Ringwood, Victoria, Australia) with 400-ps FWHM pulse width was used for ion detection. The detector output signal passes through a preamplifier stage (ZX60-P103LN+, MiniCircuits Brooklyn, NY) before a PCIe time to digital converter with 500-ps time resolution (TimeTagger4-2G, Cronologic). A start trigger synchronized with the pushout initiates acquisition with 500-ps time sampling across the time interval sufficient to capture 1 to 240 m/z (12 μs). Multiple TOF spectra recorded for each pixel were summed and saved to a data file using a

modified version of MiniSIMS v2.0.14 (Scientific Analysis Instruments, Manchester, UK), which was also used for stage control. A Dell Precision 5000 series desktop computer (Xenon E5–1650 3.5 GHz, 32 GB 2133 MHz DDR4, 512 GB SATA3 SSD) running Windows 7 enterprise was used. System sensitivity was assessed over time by measuring the count rate of ^{98}Mo per nA of primary ion current using a pre-sputtered region of molybdenum foil (Ted Pella, Redding, CA). Initial design and prototype construction of the sample load lock, analysis chamber, secondary ion optics, and TOF were done in collaboration with Scientific Analysis Instruments (Manchester, UK). Current commercial MIBI-TOF instrumentation is being manufactured by IonPath Inc. (Menlo Park, CA).

From the outset of designing the instrument, our goal was to construct a secondary ion optical column (SIO) and TOF analyzer that would maximize ion transmission while achieving sufficient mass resolution and energy filtering for quantifying nominally spaced elemental reporters with minimal interference from polyatomic species. Along these lines, the outline below describes the collection efficiency and transmission of core components of the SIO and TOF, starting from the point of ion generation at the sample:

1) Ion emittance and SIO acceptance: Given the known energy and angular distribution of sputtered secondary ions produced using primary ion energy and 45 degree incident angle (51), 90% ion collection efficiency can be achieved when using an extraction field of approximately 50 V/mm.

2) Electrostatic analyzer (ESA) tuning and design: After transiting the initial extraction electrode, secondary ions pass through an ESA in a non-dispersive configuration that places the secondary ion beam crossover at halfway between the entrance and exit. Under these conditions, an energy acceptance to be 20 eV (FWHM) is observed.

3) Ortho-TOF pushout region and energy acceptance: After exiting the ESA and passing through the second stage of the SIO, secondary ions enter the ortho-TOF through a relatively large entrance aperture sufficient to accommodate nearly all ions exiting the ESA. Prior to entering the TOF, the secondary ions are decelerated to 60 eV, such that ions within the mass range of greatest interest (89–180) enter with median velocities between approximately 8–12 mm/ μsec . At 80KHz repetition rate, approximately 25% of entering ions in this mass range are orthogonally accelerated. A discrete dynode with a detection plate 30 mm in width permits collection of this ion flux with 40 eV energy acceptance, such that nearly all ions successfully transiting the reflectron are detected.

4) Dynamic emittance matching: Uniform ion extraction across larger field sizes is achieved using dynamic emittance matching (DEM). Without DEM operation, the uniform ion optical gate is typically 250 μm in diameter. With DEMs, uniform field sizes approaching 1 mm^2 can be achieved.

Gold slide preparation

Superfrost and glass slides (Electron Microscopy Sciences, Hatfield, PA) were soaked in water with 0.1% SDS and rinsed extensively with distilled water and then acetone (Avantor-Macron Fine Chemicals, Center Valley, PA). Acetone was immediately evaporated under a stream of air to avoid trace of residues. Slides were coated with tantalum (Ta; 30-nm coating) and gold (Au; 100 nm). The slides were placed 10 at a time in adjustable rails in an electron beam evaporation station and pumped down for about 2 hours before deposition. The base pressure before the deposition was $\sim 4 \times 10^{-7}$ torr. The distance between the source and the substrate was 30 cm. Ta was evaporated

at a rate of ~ 1 nm/s. Au was evaporated immediately after at a rate of 10 to 15 $\text{\AA}/\text{s}$. Gold-coated slides were silanized in acetone with 3-aminopropyltriethoxysilane for 30 min and then washed with acetone and air-dried (Vactabond, Burlingame, CA). Slides were baked at 70 $^{\circ}\text{C}$ for 30 min and kept dry at room temperature until use.

Antibody conjugation

A summary of antibodies, reporter isotopes, and concentrations is described for each experiment in table S3. Metal-conjugated primary antibodies were prepared as described previously (31). Following labeling, antibodies were diluted in Candor PBS Antibody Stabilization solution (Candor Bioscience GmbH, Wangen, Germany) to 0.2 mg/ml and stored long term at 4 $^{\circ}\text{C}$.

Staining

Tissue sections (4 μm thick) were cut from FFPE tissue blocks using a microtome and mounted on silanized-gold slides for MIBI analysis. Slide tissue sections were baked at 70 $^{\circ}\text{C}$ for 20 min. Tissue sections were deparaffinized with three washes of fresh xylene. Tissue sections were then rehydrated with successive washes of ethanol [100% (2 \times), 95% (2 \times), 80% (1 \times), and 70% (1 \times)] and distilled water. Washes were performed using Leica ST4020 Linear Stainer (Leica Biosystems, Wetzlar, Germany) programmed to three dips per wash for 30 s each. The sections were then immersed in epitope retrieval buffer [Target Retrieval Solution (pH 9); DAKO Agilent, Santa Clara, CA], incubated at 97 $^{\circ}\text{C}$ for 40 min, and cooled down to 65 $^{\circ}\text{C}$ using Lab Vision PT Module (Thermo Fisher Scientific, Waltham, MA). Slides were washed with a wash buffer made with PBS IHC Tween buffer (Cell Marque, Rocklin, CA) containing 0.1% (w/v) bovine serum albumin (Thermo Fisher Scientific, Waltham, MA). Endogenous avidin, biotin binding proteins were blocked using Avidin/Biotin Blocking Systems (BioLegend, San Diego, CA). Sections were treated successively with avidin and biotin blocking solutions for 10 min and washed for 5 min in wash buffer. Sections were then blocked for 1 hour with 3% (v/v) donkey serum (Sigma-Aldrich, St. Louis, MO) diluted in tris-buffered saline (TBS) IHC wash buffer (Cell Marque, Rocklin, CA). Metal-conjugated antibody mix was prepared in 3% (v/v) donkey serum TBS IHC wash buffer and filtered using centrifugal filter, 0.1- μm polyvinylidene difluoride membrane (Ultrafree-MC, Merck Millipore, Tullagreen Carrigtowhill, Ireland). All experiments were stained using two antibody mixes. The first antibody mix was incubated overnight at 4 $^{\circ}\text{C}$ in humid chamber. The second mix contained antibodies of structural genes with strong signal and an anti-biotin antibody. After overnight incubation, slides were washed on an orbital shaker for 5 min in wash buffer. The second antibody mix was then applied and incubated for 1 hour at 4 $^{\circ}\text{C}$. Slides were then washed twice for 5 min in wash buffer and fixed for 5 min in a 2% diluted glutaraldehyde solution 2% (Electron Microscopy Sciences, Hatfield, PA) in low-barium PBS. Slides were rinsed briefly in low-barium PBS. Tissue sections were dehydrated with successive washes of 0.1 M tris (pH 8.5) (3 \times), distilled water (2 \times), and ethanol [70% (1 \times), 80% (1 \times), 95% (2 \times), and 100% (2 \times)]. Slides were immediately dried in a vacuum chamber for at least 1 hour before imaging. In some experiments, tissue sections were counterstained with 1 \times Hematoxylin Harris solution (Sigma) or 0.4% uranyl acetate (Electron Microscopy Sciences, Hatfield, PA) for 1 min and rinsed briefly in deionized water. Tissue sections were dehydrated with successive washes of 0.1 M tris (pH 8.5) (3 \times), distilled water (2 \times), and ethanol [70% (1 \times), 80% (1 \times), 95% (2 \times), and 100% (2 \times)].

Slides were immediately dried in a vacuum chamber for at least 1 hour before imaging.

Sensitivity measurements using CD45 conjugates

Anti-human CD45 (clone D9M8I, CST) was conjugated to one isotope from each of the metals routinely used in MIBI-TOF experiments (table S1), and each conjugate was used to stain serial sections of human FFPE tonsil sections as described above. From each section, a 100- μm FOV was imaged by MIBI-TOF. A total of 40 depths was acquired to ensure that the entire depth of the tissue was scanned. Following imaging, the remaining tissue was dissolved in a low volume of 10% trace metal-grade nitric acid. Extracted samples were volume-normalized with 1% trace metal-grade nitric acid with an equal volume of tuning solution (Fluidigm Sciences) added as an internal standard with an addition of 20 nM trace metal-grade YCl_3 (Sigma-Aldrich). Samples were run in solution on a CyTOF 2 mass cytometer (Fluidigm Sciences), and the tissue-extracted elemental isotope concentration was calculated against a blank sample using an 89Y plus tuning solution standard curve generated at the same time. The total number of reporter atoms in the sample was then calculated on the basis of the volume of the tissue-extracted solution. Sensitivity was calculated by comparing the total number of counts detected by MIBI-TOF and the absolute solution quantification, normalized to the tissue area used for both measurements. The number of antibodies needed for detection was calculated under the assumption of ~ 100 metal atoms per antibody (32).

GaAs measurements

Gallium arsenide (GaAs) semiconductor wafer (Silicon Valley Microelectronics) was cleaved and mounted on a gold slide using double-sided carbon tape (Ted Pella Inc.). A 300- μm FOV of GaAs was pre-sputtered for 5 min using a primary current of 500 nA. All primary current measurements were performed via Faraday cup (FC). Accurate current measurements by FC can be performed as low as 1 to 2 pA. However, with the instrument tuned for maximum ion transmission, the count rate of gallium exceeds the capacity of the counting system (100 Kcps) using only 100 pA. With this in mind, the secondary ion optics were tuned to attenuate the total ion flux entering the TOF such that the gallium count rate remained within the linear range of the counting system when using primary beam currents across a four log range (4 pA to 46 nA). Acquisition times for each primary current value are listed as follows: 930 pA to 45 nA: 65 s; 396 pA: 3 min, 17 s; 44 pA: 8 min, 44 s; 4 pA: 32 min, 50 s.

Sensitivity comparison between NanoSIMS and MIBI-TOF

To compare the sensitivity of MIBI-TOF and NanoSIMS 50L, the ion count rate for ^{98}Mo was quantified using a molybdenum foil standard (Ted Pella). For NanoSIMS measurements, a 100- μm FOV was pre-sputtered for 10 min using 2-nA O^- primary ion current. To maximize ion transmission and thus sensitivity, entrance slit ESO was used. The ion count rate at 98 m/z was measured using 200-pA primary ion current. For MIBI-TOF, a 200- μm FOV was pre-sputtered for 1 min using 20-nA O_2^+ . The ESA was tuned for maximal ion transmission using a voltage gap of 262 V. The ion count rate at 98 m/z was subsequently measured using 50-pA primary ion current.

Computational analysis

Image processing for all data included background subtraction and denoising as previously described (26). Cells were segmented using

deepCell (52), expression per cell was calculated as arcsinh of the counts divided by the cell area in pixels, and cells were clustered using FlowSOM (44). Cell type classification and spatial enrichment analysis was performed as previously described (26).

Image cytometry

In the analysis of β -catenin subcellular localization in colorectal carcinoma (Fig. 4, H to J), we imaged a tissue microarray stained with 34 antibodies (table S3) selected to identify relevant changes in tumor and immune cell phenotypes. Cell nuclei were segmented as described (26), and nuclei were expanded 10 pixels to generate an annulus around each nuclei for cytoplasmic signal detection. FCS files of nuclear and cytoplasmic expression of each marker (normalized to total region area) were generated. Cytobank was used for population gating of tumor cells (PanCK^+ or ECAD^+), β -catenin $^+$ cells, and cells with high and low NC ratios of β -catenin. GraphPad Prism was used for comparison of mean marker expression between NC high and low populations and determination of significance using the Mann-Whitney test.

SUPPLEMENTARY MATERIALS

Supplementary material for this article is available at <http://advances.sciencemag.org/cgi/content/full/5/10/eaax5851/DC1>

Fig. S1. MIBI-TOF is structurally designed for high-throughput, highly multiplexed imaging with high sensitivity and low noise.

Fig. S2. Thirty-six-plex staining using MIBI-TOF.

Fig. S3. MIBI-TOF can sensitively image across the elemental spectrum and allows customized ion dose/area to detect antigens with varying abundances.

Fig. S4. Evaluation of observed and expected regional distribution of tumor and immune subtypes within a single patient.

Table S1. Sensitivity measurements.

Table S2. Imaging conditions.

Table S3. Tissues and antibodies.

Movie S1. Depth profile of melanoma.

REFERENCES AND NOTES

1. L. L. De Matos, D. C. Trufelli, M. G. L. De Matos, M. A. De Silva Pinhal, Immunohistochemistry as an important tool in biomarkers detection and clinical practice. *Biomark. Insights* **5**, 9–20 (2010).
2. I. Tirosh, B. Izar, S. M. Prakadan, M. H. Wadsworth II, D. Treacy, J. J. Trombetta, A. Rotem, C. Rodman, C. Lian, G. Murphy, M. Fallahi-Sichani, K. Dutton-Regester, J.-R. Lin, O. Cohen, P. Shah, D. Lu, A. S. Genshaft, T. K. Hughes, C. G. K. Ziegler, S. W. Kazer, A. Gaillard, K. E. Kolb, A.-C. Villani, C. M. Johannessen, A. Y. Andreev, E. M. Van Allen, M. Bertagnolli, P. K. Sorger, R. J. Sullivan, K. T. Flaherty, D. T. Frederick, J. Jané-Valbuena, C. H. Yoon, O. Rozenblatt-Rosen, A. K. Shalek, A. Regev, L. A. Garraway, Dissecting the multicellular ecosystem of metastatic melanoma by single-cell RNA-seq. *Science* **352**, 189–196 (2016).
3. S. Chevrier, J. H. Levine, V. R. T. Zanotelli, K. Silina, D. Schulz, M. Bacac, C. H. Ries, L. Ailles, M. A. S. Jewett, H. Moch, M. van den Broek, C. Beisel, M. B. Stadler, C. Gedy, B. Reis, D. Pe'er, B. Bodenmiller, An immune atlas of clear cell renal cell carcinoma. *Cell* **169**, 736–749.e18 (2017).
4. M. Angelo, S. C. Bendall, R. Finck, M. B. Hale, C. Hitzman, A. D. Borowsky, R. M. Levenson, J. B. Lowe, S. D. Liu, S. Zhao, Y. Natkunam, G. P. Nolan, Multiplexed ion beam imaging of human breast tumors. *Nat. Med.* **20**, 436–442 (2014).
5. C. Giesen, H. A. O. Wang, D. Schapiro, N. Zivanovic, A. Jacobs, B. Hattendorf, P. J. Schöffler, D. Grolmund, J. M. Buhmann, S. Brandt, Z. Varga, P. J. Wild, D. Günther, B. Bodenmiller, Highly multiplexed imaging of tumor tissues with subcellular resolution by mass cytometry. *Nat. Methods* **11**, 417–422 (2014).
6. K. H. Chen, A. N. Boettiger, J. R. Moffitt, S. Wang, X. Zhuang, Spatially resolved, highly multiplexed RNA profiling in single cells. *Science* **348**, aaa6090 (2015).
7. A. F. Coskun, L. Cai, Dense transcript profiling in single cells by image correlation decoding. *Nat. Methods* **13**, 657–660 (2016).
8. W. Huang, K. Hennrick, S. Drew, A colorful future of quantitative pathology: Validation of Vectra technology using chromogenic multiplexed immunohistochemistry and prostate tissue microarrays. *Hum. Pathol.* **44**, 29–38 (2013).
9. E. C. Stack, C. Wang, K. A. Roman, C. C. Hoyt, Multiplexed immunohistochemistry, imaging, and quantitation: A review, with an assessment of Tyramide signal amplification, multispectral imaging and multiplex analysis. *Methods* **70**, 46–58 (2014).

10. J. H. Lee, E. R. Daugherty, J. Scheiman, R. Kalhor, J. L. Yang, T. C. Ferrante, R. Terry, S. S. F. Jeanty, C. Li, R. Amamoto, D. T. Peters, B. M. Turczyk, A. H. Marblestone, S. A. Inverso, A. Bernard, P. Mali, X. Rios, J. Aach, G. M. Church, Highly multiplexed subcellular RNA sequencing in situ. *Science* **343**, 1360–1363 (2014).
11. J. A. Weinstein, A. Regev, F. Zhang, DNA Microscopy: Optics-free spatio-genetic imaging by a stand-alone chemical reaction. *Cell* **178**, 229–241.e16 (2019).
12. J. R. Moffitt, D. Bambach-Mukku, S. W. Eichhorn, E. Vaughn, K. Shekhar, J. D. Perez, N. D. Rubinstein, J. Hao, A. Regev, C. Dulac, X. Zhuang, Molecular, spatial, and functional single-cell profiling of the hypothalamic preoptic region. *Science* **362**, eaau5324 (2018).
13. X. Wang, W. E. Allen, M. A. Wright, E. L. Sylvestrak, N. Samusik, S. Vesuna, K. Evans, C. Liu, C. Ramakrishnan, J. Liu, G. P. Nolan, F.-A. Bava, K. Deisseroth, Three-dimensional intact-tissue sequencing of single-cell transcriptional states. *Science* **361**, eaat5691 (2018).
14. S. K. Saka, Y. Wang, J. Y. Kishi, A. Zhu, Y. Zeng, W. Xie, K. Kirli, C. Yapp, M. Cicconet, B. J. Bellevue, S. W. Lapan, S. Yin, M. Lin, E. S. Boyden, P. S. Kaeser, G. Pihan, G. M. Church, P. Yin, Immuno-SABER enables highly multiplexed and amplified protein imaging in tissues. *Nat. Biotechnol.* **37**, 1080–1090 (2019).
15. Y. Wang, J. B. Woehrstein, N. Donoghue, M. Dai, M. S. Avendaño, R. C. J. Schackmann, J. J. Zoeller, S. S. H. Wang, P. W. Tillberg, D. Park, S. W. Lapan, E. S. Boyden, J. S. Brugge, P. S. Kaeser, G. M. Church, S. S. Agasti, R. Jungmann, P. Yin, Rapid sequential in situ multiplexing with DNA exchange imaging in neuronal cells and tissues. *Nano Lett.* **17**, 6131–6139 (2017).
16. S. S. Agasti, Y. Wang, F. Schueder, A. Sukumar, R. Jungmann, P. Yin, DNA-barcoded labeling probes for highly multiplexed Exchange-PAINT imaging. *Chem. Sci.* **8**, 3080–3091 (2017).
17. G. Gut, M. D. Herrmann, L. Pelkmans, Multiplexed protein maps link subcellular organization to cellular states. *Science* **361**, eaar7042 (2018).
18. J.-R. Lin, B. Izar, S. Wang, C. Yapp, S. Mei, P. M. Shah, S. Santagata, P. K. Sorger, Highly multiplexed immunofluorescence imaging of human tissues and tumors using t-CyCIF and conventional optical microscopes. *eLife* **7**, e31657 (2018).
19. M. J. Gerdes, C. J. Sevinsky, A. Sood, S. Adak, M. O. Bello, A. Bordwell, A. Can, A. Corwin, S. Dinn, R. J. Filkins, D. Hollman, V. Kamath, S. Kaanumalle, K. Kenny, M. Larsen, M. Lazare, Q. Li, C. Lowes, C. C. McCulloch, E. McDonough, M. C. Montalto, Z. Pang, J. Rittscher, A. Santamaria-Pang, B. D. Sarachan, M. L. Seel, A. Seppo, K. Shaikh, Y. Sui, J. Zhang, F. Ginty, Highly multiplexed single-cell analysis of formalin-fixed, paraffin-embedded cancer tissue. *Proc. Natl. Acad. Sci. U.S.A.* **110**, 11982–11987 (2013).
20. R. L. Hervig, F. K. Mazdab, P. Williams, Y. Guan, G. R. Huss, L. A. Leshin, Useful ion yields for Cameca IMS 3f and 6f SIMS: Limits on quantitative analysis. *Chem. Geol.* **227**, 83–99 (2006).
21. R. G. Wilson, SIMS quantification in Si, GaAs, and diamond - an update. *Int. J. Mass Spectrom. Ion Process.* **143**, 43–49 (1995).
22. T. Wirtz, N. Vanhove, L. Pillatsch, D. Dowsett, S. Sijbrandij, J. Notte, Towards secondary ion mass spectrometry on the helium ion microscope: An experimental and simulation based feasibility study with He⁺ and Ne⁺ bombardment. *Appl. Phys. Lett.* **101**, 041601 (2012).
23. R. G. Wilson, F. A. Stevie, C. W. Magee, *Secondary ion mass spectrometry: A Practical Handbook for Depth Profiling and Bulk Impurity Analysis* (Wiley, 1989).
24. J. C. Vickerman, D. Briggs, *TOF-SIMS: Materials Analysis by Mass Spectrometry* (IM Publications, 2013).
25. M. Jamal-Hanjani, G. A. Wilson, N. McGranahan, N. J. Birkbak, T. B. K. Watkins, S. Veeriah, S. Shafi, D. H. Johnson, R. Mitter, R. Rosenthal, M. Salm, S. Horswell, M. Escudero, N. Matthews, A. Rowan, T. Chambers, D. A. Moore, S. Turajlic, H. Xu, S. M. Lee, M. D. Forster, T. Ahmad, C. T. Hiley, C. Abbosh, M. Falzon, E. Borg, T. Marafioti, D. Lawrence, M. Hayward, S. Kolvekar, N. Panagiotopoulos, S. M. Janes, R. Thakrar, A. Ahmed, F. Blackhall, Y. Summers, R. Shah, L. Joseph, A. M. Quinn, P. A. Crosbie, B. Naidu, G. Middleton, G. Langman, S. Trotter, M. Nicolson, H. Remmen, K. Kerr, M. Chetty, L. Gomersall, D. A. Fennell, A. Nakas, S. Rathinam, G. Anand, S. Khan, P. Russell, V. Ezhil, B. Ismail, M. Irvin-Sellers, V. Prakash, J. F. Lester, M. Kornaszewska, R. Attanoos, H. Adams, H. Davies, S. Dentre, P. Taniere, B. O'Sullivan, H. L. Lowe, J. A. Hartley, N. Iles, H. Bell, Y. Ngai, J. A. Shaw, J. Herrero, Z. Szallasi, R. F. Schwarz, A. Stewart, S. A. Quezada, J. Le Quesne, P. Van Loo, C. Dive, A. Hackshaw, C. Swanton; TRACERx Consortium, Tracking the evolution of non-small-cell lung cancer. *N. Engl. J. Med.* **376**, 2109–2121 (2017).
26. L. Keren, M. Bosse, D. Marquez, R. Angoshtari, S. Jain, S. Varma, S.-R. Yang, A. Kurian, D. Van Valen, R. West, S. C. Bendall, M. Angelo, A structured tumor-immune microenvironment in triple negative breast cancer revealed by multiplexed ion beam imaging. *Cell* **174**, 1373–1387.e19 (2018).
27. C. Lechene, F. Hillion, G. McMahon, D. Benson, A. M. Kleinfeld, J. P. Kampf, D. Distel, Y. Luyten, J. Bonventre, D. Hentschel, K. M. Park, S. Ito, M. Schwartz, G. Benichou, G. Slodzin, High-resolution quantitative imaging of mammalian and bacterial cells using stable isotope mass spectrometry. *J. Biol.* **5**, 20 (2006).
28. D.-S. Zhang, V. Piazza, B. J. Perrin, A. K. Rzedzinska, J. C. Poczatek, M. Wang, H. M. Prosser, J. M. Ervasti, D. P. Corey, C. P. Lechene, Multi-isotope imaging mass spectrometry reveals slow protein turnover in hair-cell stereocilia. *Nature* **481**, 520–524 (2012).
29. K. Wittmaack, On the mechanism of cluster emission in sputtering. *Phys. Lett. A* **69**, 322–325 (1979).
30. D. R. Bandura, V. I. Baranov, O. I. Ornatsky, A. Antonov, R. Kinach, X. Lou, S. Pavlov, S. Vorobiev, J. E. Dick, S. D. Tanner, Mass cytometry: Technique for real time single cell multitarget immunoassay based on inductively coupled plasma time-of-flight mass spectrometry. *Anal. Chem.* **81**, 6813–6822 (2009).
31. S. C. Bendall, E. F. Simonds, P. Qiu, E.-a. D. Amir, P. O. Krutzik, R. Finck, R. V. Bruggner, R. Melamed, A. Trejo, O. I. Ornatsky, R. S. Balderas, S. K. Plevritis, K. Sachs, D. Pe'er, S. D. Tanner, G. P. Nolan, Single-cell mass cytometry of differential immune and drug responses across a human hematopoietic continuum. *Science* **332**, 687–696 (2011).
32. X. Lou, G. Zhang, I. Herrera, R. Kinach, O. Ornatsky, V. Baranov, M. Nitz, M. A. Winnik, Polymer-based elemental tags for sensitive bioassays. *Angew. Chemie Int. Ed.* **46**, 6111–6114 (2007).
33. R. Milo, P. Jorgensen, U. Moran, G. Weber, M. Springer, BioNumbers—The database of key numbers in molecular and cell biology. *Nucleic Acids Res.* **38**, D750–D753 (2010).
34. A. A. Khan, J. G. Quigley, Control of intracellular heme levels: Heme transporters and heme oxygenases. *Biochim. Biophys. Acta* **1813**, 668–682 (2011).
35. M. R. Emmert-Buck, R. F. Bonner, P. D. Smith, R. F. Chuaiqui, Z. Zhuang, S. R. Goldstein, R. A. Weiss, L. A. Liotta, Laser capture microdissection. *Science* **274**, 998–1001 (1996).
36. E. Bártová, J. Krejčí, A. Harnicarová, G. Galiová, S. Kozubek, Histone modifications and nuclear architecture: A review. *J. Histochem. Cytochem.* **56**, 711–721 (2008).
37. S. C. C. Wong, E. S. F. Lo, A. K. C. Chan, K. C. Lee, W. L. Hsiao, Nuclear β catenin as a potential prognostic and diagnostic marker in patients with colorectal cancer from Hong Kong. *Mol. Pathol.* **56**, 347–352 (2003).
38. P. Y. Cheah, P. H. Choo, J. Yao, K. W. Eu, F. Seow-Choen, A survival-stratification model of human colorectal carcinomas with β -catenin and p27^{kip1}. *Cancer* **95**, 2479–2486 (2002).
39. P. J. Morin, β -catenin signaling and cancer. *Bioessays* **21**, 1021–1030 (1999).
40. M. Soichot, B. Hennart, A. Al Saabi, A. Leloire, P. Froguel, C. Levy-Marchal, O. Poulain-Godefroy, D. Allorge, Identification of a variable number of tandem repeats polymorphism and characterization of LEF-1 response elements in the promoter of the *IDO1* gene. *PLOS ONE* **6**, e25470 (2011).
41. A. Herbst, V. Jurinovic, S. Krebs, S. E. Thieme, H. Blum, B. Göke, F. T. Kolligs, Comprehensive analysis of β -catenin target genes in colorectal carcinoma cell lines with deregulated Wnt/ β -catenin signaling. *BMC Genomics* **15**, 74 (2014).
42. A. Kaidi, A. C. Williams, C. Paraskeva, Interaction between β -catenin and HIF-1 promotes cellular adaptation to hypoxia. *Nat. Cell Biol.* **9**, 210–217 (2007).
43. W. Zhang, X. Shi, Y. Peng, M. Wu, P. Zhang, R. Xie, Y. Wu, Q. Yan, S. Liu, J. Wang, HIF-1 α promotes epithelial-mesenchymal transition and metastasis through direct regulation of ZEB1 in colorectal cancer. *PLOS ONE* **10**, e0129603 (2015).
44. S. Van Gassen, B. Callebaut, M. J. Van Helden, B. N. Lambrecht, P. Demeester, T. Dhaene, Y. Saey, FlowSOM: Using self-organizing maps for visualization and interpretation of cytometry data. *Cytometry A* **87**, 636–645 (2015).
45. F. Andre, M. V. Dieci, P. Dubsky, C. Sotiriou, G. Curigliano, C. Denkert, S. Loi, Molecular pathways: Involvement of immune pathways in the therapeutic response and outcome in breast cancer. *Clin. Cancer Res.* **19**, 28–33 (2013).
46. C. Denkert, S. Loibl, A. Noske, M. Roller, B. M. Müller, M. Komor, J. Budczies, S. Darb-Esfahani, R. Kronenwett, C. Hanusch, C. von Törne, W. Weichert, K. Engels, C. Solbach, I. Schrader, M. Dietel, G. von Minckwitz, Tumor-associated lymphocytes as an independent predictor of response to neoadjuvant chemotherapy in breast cancer. *J. Clin. Oncol.* **28**, 105–113 (2010).
47. M. L. Disis, S. E. Stanton, Triple-negative breast cancer: Immune modulation as the new treatment paradigm. *Am. Soc. Clin. Oncol. Educ. Book* **35**, e25–e30 (2015).
48. M. W. L. Teng, S. F. Ngiew, A. Ribas, M. J. Smyth, Classifying cancers based on T-cell infiltration and PD-L1. *Cancer Res.* **75**, 2139–2145 (2015).
49. A. P. Frei, F. A. Bava, E. R. Zunder, E. W. Hsieh, S. Y. Chen, G. P. Nolan, P. F. Gherardini, Highly multiplexed simultaneous detection of RNAs and proteins in single cells. *Nat. Methods* **13**, 269–275 (2016).
50. D. Schulz, V. R. T. Zanotelli, J. R. Fischer, D. Schapiro, S. Engler, X. K. Lun, H. W. Jackson, B. Bodenmiller, Simultaneous multiplexed imaging of mRNA and proteins with subcellular resolution in breast cancer tissue samples by mass cytometry. *Cell Syst.* **6**, 25–36.e5 (2018).
51. K. Wittmaack, Secondary-ion emission from silicon bombarded with atomic and molecular noble-gas ions. *Surf. Sci.* **90**, 557–563 (1979).
52. D. A. Van Valen, T. Kudo, K. M. Lane, D. N. Macklin, N. T. Quach, M. M. DeFelice, I. Maayan, Y. Tanouchi, E. A. Ashley, M. W. Covert, Deep learning automates the quantitative analysis of individual cells in live-cell imaging experiments. *PLOS Comput. Biol.* **12**, e1005177 (2016).

Acknowledgments: We thank P. Blenkinsopp for expertise and technical support in developing this instrument. Slide preparation was performed at the Stanford Nano Shared Facility (SNSF), supported by the NSF, under award ECCS-1542152. We also thank T. Carver from the Microfab Shop of SNSF for helpful technical advice and for the thin-film evaporation services, A. Lako and S. Rodig from the Dana-Farber Cancer Institute for control samples, and D. Glass and S. Greenbaum for comments. **Funding:** L.K. was a Damon Runyon Fellow supported by the Damon Runyon Cancer Research Foundation (DRG-2292-17) and a non-stipendiary awardee of the EMBO Long-Term fellowship (ALTF 1128–2016). T.R. was supported by NIH 5-T32-AI07290–33. E.M. was supported by the NSF Graduate Research Fellowship (grant no. 2017242837). G.N. was supported by grant W81XWH-14-1-0180 from the DoD. R.W. was supported by NIH 5R01CA18390402. K.V. and T.J.M. were supported by Udall grant NS062684. S.C.B. was supported by a gift from Christy and Bill Neidig, the Damon Runyon Cancer Research Foundation (DRG-2017-09), and the NIH (1DP2OD022550, 1-R00-GM104148, 5U19AI116484, and U19 AI104209). M.A. was supported by 1-DP5-OD019822. S.C.B., M.A., and T.J.M. were jointly supported by 1R01AG056287 and 1R01AG057915. S.C.B. and M.A. were jointly supported by 1U24CA224309, the Bill and Melinda Gates Foundation, and a Translational Research Award from the Stanford Cancer Institute. S.J.G. was supported by U19 AI104209, R01 AR067145, and R01 AI32494. **Author contributions:** L.K. analyzed the data and wrote the manuscript. M.B. performed the experiments. M.A., S.C.B., and S.T. designed the instrument. M.B. and D.K. maintained the instrument. T.R. performed subcellular analysis (Fig. 4, H to J). K.V. performed brain experiments (Fig. 1M). E.M. analyzed Fe signal (Fig. 3). N.F.G. analyzed time-dependent signal

(Fig. 4E). D.M., R.A., H.F., and J.W. performed experiments. N.K., R.W., T.J.M., and S.J.G. provided samples and consulted on tissue pathology. G.N., T.J.M., and S.J.G. supported the work. S.C.B. and M.A. conceived and supervised the work. **Competing interests:** M.A., S.C.B., and G.N. are inventors on patent US20150287578A1. M.A. and S.C.B. are board members and shareholders in IonPath Inc. G.N. is a shareholder in IonPath Inc. H.F. is a shareholder and employee of IonPath Inc. E.M. and T.R. are consultants for IonPath Inc. All other authors declare no competing interests. **Data and materials availability:** All data needed to evaluate the conclusions in the paper are present in the paper and/or the Supplementary Materials. All the data described in this work can be accessed through a web interface and downloaded at <https://mibi-share.ionpath.com>. The code for the analysis can be downloaded at <https://github.com/lkeren/MibiAnalysis>. Cell segmentation can be performed at www.deepcell.org.

Submitted 4 April 2019

Accepted 14 September 2019

Published 9 October 2019

10.1126/sciadv.aax5851

Citation: L. Keren, M. Bosse, S. Thompson, T. Risom, K. Vijayaragavan, E. McCaffrey, D. Marquez, R. Angoshtari, N. F. Greenwald, H. Fienberg, J. Wang, N. Kambham, D. Kirkwood, G. Nolan, T. J. Montine, S. J. Galli, R. West, S. C. Bendall, M. Angelo, MIBI-TOF: A multiplexed imaging platform relates cellular phenotypes and tissue structure. *Sci. Adv.* **5**, eaax5851 (2019).